Electronic ISSN: 1309-0267

International Journal of Engineering & Applied Sciences

IJEAS

I J E A S

Volume 11, Issue 4
2019

Published by Akdeniz University

Editorial Board

(The name listed below is not Alphabetical or any title scale)

Abstracting & Indexing

IJEAS provides unique **DOI** link to every paper published.

Editorial Scope

The journal presents its readers with broad coverage across some branches of engineering and science of the latest development and application of new solution algorithms, artificial intelligent techniques innovative numerical methods and/or solution techniques directed at the utilization of computational methods in solid and nano-scaled mechanics.

International Journal of Engineering & Applied Sciences (IJEAS) is an Open Access Journal

International Journal of Engineering & Applied Sciences (IJEAS) publish original contributions on the following topics:

Numerical Methods in Solid Mechanics

Nanomechanic and applications

Microelectromechanical systems (MEMS)

Vibration Problems in Engineering

Higher order elasticity (Strain gradient, couple stress, surface elasticity, nonlocal elasticity) Applied Mathematics

CONTENTS

International Journal of Engineering & Applied Sciences (IJEAS)
Vol.11, Issue 4 (2019) 455-467
http://dx.doi.org/10.24107/ijeas.644160
Int J Eng Appl Sci 11(4) (2019) 455-467

Higher Order Fitted Operator Finite Difference Method for Two-Parameter Parabolic Convection-Diffusion Problems

Tesfaye Aga Bullo [1], Gemechis File Duressa [2], Guy Aymard Degla [3]*

[1,2] Department of Mathematics, Jimma University, Jimma, P.O. Box 378, Ethiopia
[3] Institut De Mathematiques et de sciences physiques, Universit D'Abomey Calavi, Benin

E-mail address: tesfayeaga2@gmail.com [1]*, gammeef@gmail.com [1], gdegla@gmail.com [2]

ORCID numbers of authors:
0000-0001-6766-4803[1], 0000-0003-1889-4690[2], 0000-0003-1162-6140[3]*

Received date: 07.11.2019
Accepted date: 24.11.2019

Abstract

In this paper, we consider singularly perturbed parabolic convection-diffusion initial boundary value problems with two small positive parameters to construct higher order fitted operator finite difference method. At the beginning, we discretize the solution domain in time direction to approximate the derivative with respect to time and considering average levels for other terms that yields two point boundary value problems which covers two time level. Then, full discretization of the solution domain followed by the derivatives in two point boundary value problem are replaced by central finite difference approximation, introducing and determining the value of fitting parameter ended at system of equations that can be solved by tri-diagonal solver. To improve accuracy of the solution with corresponding higher orders of convergence, we applying Richardson extrapolation method that accelerates second order to fourth order convergent. Stability and consistency of the proposed method have been established very well to assure the convergence of the method. Finally, validate by considering test examples and then produce numerical results to care the theoretical results and to establish its effectiveness. Generally, the formulated method is stable, consistent and gives more accurate numerical solution than some methods existing in the literature for solving singularly perturbed parabolic convection- diffusion initial boundary value problems with two small positive parameters.

Keywords: Singularly perturbation parabolic problems, two parameters, fitted operator, accurate solution.

1. Introduction

Singularly perturbed parabolic convection–diffusion problems appeared as model in various branches of science and engineering such as modeling of water quality problems in river networks, fluid flow at high Reynold's numbers, convective heat transport problem, drift diffusion equation of semiconductor device modeling, electromagnetic field problem in moving media, financial modeling and turbulence model, one can refer [1, 4, 5, 6, 8, 11]. As stated in book written by Morton [7] and in article presented by Das and Mehrmann [1], singularly perturbed parabolic

problems describe the transport of solute in groundwater and surface water, the displacement of oil by fluid injection in oil recovery, the movement of aerosols and trace gases in the atmosphere, and describe fluid flow processes in many other applications. Boundary layers occur in the solution of singularly perturbed problems when the singular perturbation parameter multiplies the terms involving the highest order derivatives in the differential equation tends to zero. These boundary layers are neighborhood of the boundary of the domain, where the solution has a very steep gradient.

If one tries to solve singularly perturbed parabolic problems using standard numerical methods applied to solve partial differential equations, then very inaccurate solutions are obtained unless the mesh discretization domain used is extremely small. Even in this context, carful numerical experiments show that the classical computational methods like; standard finite difference or finite element or finite volume methods fail to decrease the maximum point-wise error as the mesh is smaller and smaller; until the mesh size and the perturbation parameter have the same order of magnitude. This contradicts the natural expectation that the error of an acceptable computational method decreases when the mesh is refined. Subsequently, the size of system of algebraic equations will be growing more as the dimension of problem increases. Hence this incorporates the huge computational cost. This drawback motivates researcher to develop and analysis numerical methods which gives accurate numerical solution corresponding to higher order of convergence. Thus, in order to get inexpensive but accurate numerical solution, it will be necessary to develop methods that can handle singular perturbation problems. Hence, numerically solving singularly perturbed parabolic problems depend upon the small positive parameters that affect highest order derivatives of the problem; solution varies rapidly in some parts of the domain and varies slowly in some other parts.

As a result, in the past few decades, various numerical schemes are proposed to solve singularly perturbed parabolic problems with two small positive parameters. For instance, from many few recently developed methods are; parameter-uniform finite element method presented by Kadalbajoo and Yadaw [4], spline difference scheme [12], robust finite difference method [8], robust layer adapted difference method [3] and a parameter-uniform higher order finite difference scheme [2]. All these works concerns singularly perturbed parabolic problems in which perturbation parameters affecting the first and second order derivative terms. While for the perturbation parameter affects only the second order derivative is other type of problem to be discussed separately in other part of our work. These developed methods analyzed very well in different approaches and produce good accurate numerical solution corresponding with first and second order rate of convergence to demonstrate efficiency of the methods.

However, the obtained approximate solution and corresponding order of convergence are not more satisfactory which indicates that yet to solve the stated problem needs develop other numerical methods to produce more accurate numerical solution. Thus, in this work, we formulate, analyze and implement higher order fitted operator finite difference method to solve singularly perturbed parabolic convection-diffusion problems with two small parameters more accurately.

2. Formulation of the Method

We consider the following singularly perturbed parabolic initial boundary value problem (IBVP) on the solution domain $(x,t) \in Q := \Omega \times (0,T],\ \Omega = (0,1)$

$$\varepsilon \frac{\partial^2 u}{\partial x^2} + \mu a(x,t) \frac{\partial u}{\partial x} - b(x,t)u(x,t) - \frac{\partial u}{\partial t} = f(x,t) \tag{1}$$

subject to the initial and boundary conditions

$$\begin{aligned} &u(x,0) = s(x),\ \ x \in \bar{\Omega} \\ &u(0,t) = q_0(t),\ \ u(1,t) = q_1(t),\ \ t \in [0,T] \end{aligned} \tag{2}$$

with two small parameters $0 < \varepsilon, \mu << 1$. The coefficient functions $a(x,t), b(x,t)$ and source function $f(x,t)$ are sufficiently regular on $\bar{Q}$ and satisfy $a(x,t) \geq \alpha > 0$, $b(x,t) \geq \beta > 0$; α and β are real numbers. Also, we assume that sufficient regularity and compatibility conditions imposed on the functions $s(x)$, $q_0(t)$, $q_1(t)$ and $f(x,t)$, so that a unique solution exists. Problem given by Eqs. (1) and (2) exhibits two boundary layer with different width depending on the relation between the two parameters ε and μ, one can see refer [1, 2, 4].

2.1. Temporal discretization

To discretize the time variable with uniform step size *k*, so that the time interval $[0,T]$ is partitioned as $0 = t_0 < t_1 < \ldots < t_N = T$ for

$$t_n = nk,\ \ k = \frac{T}{N},\ \ n = 0,1,2,\ldots,N \tag{3}$$

Now, at the point $(x, t_{n+0.5})$, Eq. (1) can be written as

$$\varepsilon \frac{\partial^2 u}{\partial x^2}(x,t_{n+0.5}) + \mu a(x,t_{n+0.5}) \frac{\partial u}{\partial x}(x,t_{n+0.5}) - b(x,t_{n+0.5})u(x,t_{n+0.5}) = \frac{\partial u}{\partial t}(x,t_{n+0.5}) + f(x,t_{n+0.5}) \tag{4}$$

Using Taylor's series expansion about the point $(x, t_{n+0.5})$, we have

$$u(x,t_{n+1}) = u(x,t_{n+0.5}) + \frac{k}{2}\frac{\partial u}{\partial t}u(x,t_{n+0.5}) + \frac{k^2}{8}\frac{\partial^2 u}{\partial t^2}u(x,t_{n+0.5}) + \frac{k^3}{48}\frac{\partial^3 u}{\partial t^3}u(x,t_{n+0.5}) + \ldots$$

$$u(x,t_n) = u(x,t_{n+0.5}) - \frac{k}{2}\frac{\partial u}{\partial t}u(x,t_{n+0.5}) + \frac{k^2}{8}\frac{\partial^2 u}{\partial t^2}u(x,t_{n+0.5}) - \frac{k^3}{48}\frac{\partial^3 u}{\partial t^3}u(x,t_{n+0.5}) + \ldots$$

which gives

$$\frac{\partial u}{\partial t}(x,t_{n+0.5}) = \frac{u(x,t_{n+1}) - u(x,t_n)}{k} + \tau_1 = \frac{u_{(x)}^{n+1} - u_{(x)}^n}{k} + \tau_1 \tag{5}$$

where $\tau_1 = -\frac{k^2}{24}\frac{\partial^3 u}{\partial t^3}u(x,t_{n+0.5}) \equiv O(k^2)$

This indicates, the error estimate of time discretization is given by

$$\left\|E_n\right\|_\infty \le Ck^2 \tag{6}$$

where $C = \frac{1}{24}\left\|\frac{\partial^3 u}{\partial t^3}u(x,t_{i+0.5})\right\|$, $t_n \le t_i \le t_{n+0.5}$, $\forall i = 1, 2, ...N$, is a constant independent of parameters ε, μ and k.

let take the average of the remaining terms in Eq. (4) which is written as

$$\begin{aligned}&\varepsilon\frac{\partial^2 u}{\partial x^2}(x,t_{n+0.5}) + \mu a(x,t_{n+0.5})\frac{\partial u}{\partial x}(x,t_{n+0.5}) - b(x,t_{n+0.5})u(x,t_{n+0.5}) - f(x,t_{n+0.5})\\ &= \frac{1}{2}\left(\left\{\varepsilon\frac{d^2u^{n+1}}{dx^2} + \mu a^{n+1}\frac{du^{n+1}}{dx} - b_{(x)}^{n+1}u_{(x)}^{n+1} - f_{(x)}^{n+1}\right\} + \left\{\varepsilon\frac{d^2u^{n}}{dx^2} + \mu a^{n+1}\frac{du^{n}}{dx} - b_{(x)}^{n}u_{(x)}^{n} - f_{(x)}^{n}\right\}\right)\end{aligned} \tag{7}$$

Substituting Eqs. (5) and (7) into Eq. (4) yields linear system of boundary value problems in space at each two time level of the form

$$\varepsilon\frac{d^2u^{n+1}}{dx^2} + \mu a^{n+1}\frac{du^{n+1}}{dx} - \left(b_{(x)}^{n+1} + \frac{2}{k}\right)u_{(x)}^{n+1} + \varepsilon\frac{d^2u^{n}}{dx^2} + \mu a^{n+1}\frac{du^{n}}{dx} - \left(b_{(x)}^{n} - \frac{2}{k}\right)u_{(x)}^{n} = f_{(x)}^{n+1} + f_{(x)}^{n} \tag{8}$$

subject to the boundary conditions at each level

$$\begin{aligned}&u(0,t_{n+1}) = q_0(t_{n+1}),\ u(1,t_{n+1}) = q_1(t_{n+1})\\ &u(0,t_n) = q_0(t_n),\ u(1,t_n) = q_1(t_n)\end{aligned} \tag{9}$$

The characteristic equation for the homogeneous part with constant coefficients α and β of Eq. (8) on $(n+1)^{th}$ time level is

$$\varepsilon r^2(x) + \mu\alpha r(x) - \left(\beta + \frac{2}{k}\right) = 0 \tag{10}$$

Assume it has two real solutions $r_1(x) < 0$ and $r_2(x) > 0$ that describe the boundary layers at $x = 0$ and $x = 1$, respectively**.** Let

$$\theta_1 = -\max_{x\in[0,1]} r_1(x) \text{ and } \theta_2 = \min_{x\in[0,1]} r_2(x)$$

The situations of two layers are characterized by the case $\mu << \varepsilon$ as $\varepsilon \to 0$, which suggests that $\theta_1 \approx \theta_2 \approx \sqrt{\frac{2+k\beta}{\varepsilon k}}$ and we have the layer like to the case $\mu \approx 0$. The other condition, layers arises across in the case where $\varepsilon << \mu$ as $\mu \to 0$ yields $\theta_1 \approx -\max_{x\in[0,1]} \frac{-\mu\alpha}{\varepsilon} = \frac{\mu\alpha}{\varepsilon}$ and $\theta_2 \approx 0$. Depending on these facts, we have the following two cases:

Case 1: if $\mu << \varepsilon$ as $\varepsilon \to 0$, Eq. (1) has two boundary layers of each width $O(\sqrt{\varepsilon})$ then the solution for homogeneous part of Eq.(8) on $(n+1)^{th}$ time level can be given by

$$u(x) = A_1 + B_1 \exp(-\sqrt{\frac{2+k\beta}{\varepsilon k}}x) \tag{11}$$

where A_1, B_1 and $b(x,t) \geq \beta > 0$ are real constant numbers.

Case 2: if $\varepsilon << \mu$ as $\mu \to 0$, Eq. (1) has two boundary layers of width $O(\frac{\varepsilon}{\mu})$ and $O(\mu)$ on the left and right sides respectively, then the solution for homogeneous part of Eq.(8) on $(n+1)^{th}$ time level can be given by

$$u(x) = A_2 + B_2 \exp(-\frac{\mu\alpha}{\varepsilon}x) \tag{12}$$

where A_2, B_2 and $a(x,t) \geq \alpha > 0$ are real constant numbers.

Here, most numerical methods gives good accurate solution for case 1, since $\mu \approx 0$, it has reaction-diffusion parabolic problem property. While for case 2 is challenging to produce good accurate solution. Thus, in this work our focuses to be treat the problem when it is in case 2.

2.2. The full discrete problem

Assume that *M* be positive integer and $\bar{\Omega}^M$ denote partition of $[0,1]$ into *M* subintervals such that $0 = x_0 < x_1 < \ldots < x_M = 1$ and $x_m = mh,\ h = \frac{1}{M},\ 1 = 0,1,2,\ldots,M$ then the tensor-product grids on $\bar{Q}^{M,N}$. Undertake the notation $U_m^n \approx u(x_m, t_n)$ and using the central finite difference approximation, Eq. (8) written as

$$\begin{aligned} &\varepsilon\frac{U_{m+1}^{n+1} - 2U_m^{n+1} + U_{m-1}^{n+1}}{h^2} + \mu a_m^{n+1}\frac{U_{m+1}^{n+1} - U_{m-1}^{n+1}}{2h} - \left(b_m^{n+1} + \frac{2}{k}\right)u_m^{n+1} + \\ &\varepsilon\frac{U_{m+1}^{n} - 2U_m^{n} + U_{m-1}^{n}}{h^2} + \mu a_m^{n}\frac{U_{m+1}^{n} - U_{m-1}^{n}}{2h} - \left(b_m^{n} - \frac{2}{k}\right)u_m^{n} = f_m^{n+1} + f_m^{n} + \tau_2 \end{aligned} \tag{13}$$

subject to the discrete initial and boundary conditions

$$\begin{aligned} &U(x_m,0)=s(x_m),\ \ x_m\in\bar{\Omega}^{[0,1]}\\ &U(0,t_{n+1})=q_0(t_{n+1}),\ \ u(1,t_{n+1})=q_1(t_{n+1}),\ \ t_{n+1}\in\left[0,T\right]^N \end{aligned} \tag{14}$$

where $\tau_2=h^2\left(\mu a_m^{n+1}\left(u_{xxx}\right)_m^{n+1}+\frac{\varepsilon}{2}\left(u_{xxxx}\right)_m^{n+1}\right)-\tau_1\equiv O\left(h^2+k^2\right)$

Let introduce fitting parameter σ on the $(n+1)^{th}$ - level of homogeneous part of Eq. (13), multiply both sides of this equation by $\frac{h}{\mu}$, denote $\rho=\frac{\mu h}{\varepsilon}$ and then evaluate limits both side gives

$$\frac{\sigma}{\rho}=-\frac{\alpha\lim\limits_{h\to 0}\left(U_{m+1}^{n+1}-U_{m-1}^{n+1}\right)}{2\lim\limits_{h\to 0}\left(U_{m+1}^{n+1}-2U_m^{n+1}+U_{m-1}^{n+1}\right)} \tag{15}$$

To determine the value of introduced fitting parameter σ, we consider the discrete form Eq. (12) that leads to

$$\lim_{h\to 0}U_m^{n+1}=A_2+B_2\exp\left(-\alpha m\rho\right) \tag{16}$$

Inducing indices from Eq. (16) for $U_{m\pm1}^{n+1}$ and substituting into Eq. (15), we get

$$\sigma=\frac{\alpha\rho}{2}\coth\left(\frac{\alpha\rho}{2}\right) \tag{17}$$

The fitted scheme of Eq. (13) can be written as three term recurrence relation in space direction and two levels in time direction as

$$E_m^{n+1}U_{m-1}^{n+1}-F_m^{n+1}U_m^{n+1}+G_m^{n+1}U_{m+1}^{n+1}=H_m^{n+1},\quad m=1,2,...,M \text{ and } n=0,1,...,N \tag{18}$$

where, $E_m^{n+1}=\frac{\varepsilon\sigma}{h^2}-\frac{\mu a_m^{n+1}}{2h}$, $F_m^{n+1}=\frac{2\varepsilon\sigma}{h^2}+b_m^{n+1}+\frac{2}{k}$, $G_m^{n+1}=\frac{\varepsilon\sigma}{h^2}+\frac{\mu a_m^{n+1}}{2h}$

and $H_m^{n+1}=f_m^{n+1}+f_m^n-\varepsilon\frac{U_{m+1}^n-2U_m^n+U_{m-1}^n}{h^2}-\mu a_m^n\frac{U_{m+1}^n-U_{m-1}^n}{2h}+\left(b_m^n-\frac{2}{k}\right)u_m^n$

Hence, scheme developed in Eq. (18) is considered as fitted operator finite difference method to solve the problem in Eqs. (1) and (2). Tri-diagonal system of Eq. (18) with respect to the *x* direction and the coefficients E_m^{n+1}, F_m^{n+1}, G_m^{n+1} and the right-hand side H_m^{n+1} are given that they satisfy the conditions $\left|E_m^{n+1}\right|>0$, $\left|F_m^{n+1}\right|>0$, $\left|G_m^{n+1}\right|>0$ and $\left|F_m^{n+1}\right|>\left|E_m^{n+1}\right|+\left|G_m^{n+1}\right|$ at each $(n+1)^{th}$ level. These situations guarantee that the system is *diagonally dominant* and it can be solved by tri-diagonal solver.

3. Richardson Extrapolation

This technique is a convergence acceleration technique which involves combination of two computed approximations of a solution. The combination goes out to be an improved approximation. In this work, the truncation terms of the schemes given in Eqs. (5) and (13), we have

$$\left|u(x_m,t_n)-U_m^n\right| \le C\left(h^2+k^2\right) \tag{19}$$

where $u(x_m,t_n)$ and U_m^n are exact and approximate solutions respectively, C is constant free from mesh sizes h and k.
Let Q_{2M}^{2N} be the mesh found by dividing each mesh interval in Q_M^N and symbolize the approximation solution on Q_{2M}^{2N} by $\bar{U}_m^n$. Consider Eq. (19) works for any $h,k \neq 0$, which implies:

$$u(x_m,t_n)-U_m^n \le C\left(h^2+k^2\right)+R_M^N, \quad (x_m,t_n)\in Q_M^N \tag{20}$$

So that, it works for any $\frac{h}{2}, \frac{k}{2} \neq 0$ yields:

$$u(x_m,t_n)-\bar{U}_m^n \le C\left(\left(\frac{h}{2}\right)^2+\left(\frac{k}{2}\right)^2\right)+R_{2M}^{2N}, \quad (x_m,t_n)\in Q_{2M}^{2N} \tag{21}$$

where the remainders, R_M^N and R_{2M}^{2N} are $O(h^4+k^4)$.
Combination of inequalities in Eqs. (20) and (21) leads to $3u(x_m,t_n)-\left(4\bar{U}_m^n-U_m^n\right)\approx O(h^4+k^4)$ which proposes that

$$\left(U_m^n\right)^{ext}=\frac{1}{3}\left(4\bar{U}_m^n-U_m^n\right) \tag{22}$$

is also approximation of $u(x_m,t_n)$. By means of this approximation to estimate the truncation error, we obtain

$$\left|u(x_m,t_n)-\left(U_m^n\right)^{ext}\right| \le C\left(h^4+k^4\right) \tag{23}$$

where C is constant free of mesh sizes h and k. Thus, the obtained accelerated method is order four convergent with respect to both independent variables.

4. Convergence analysis

The Von Neumann stability technique has been applied to investigate the stability of the developed scheme in Eq. (18), by assuming that the solution of Eq. (18) at the grid point $\left(x_m,t_n\right)$ is given by:

$$U_m^n = \xi^n e^{i\,\mathrm{m}\theta} \tag{24}$$

where $i = \sqrt{-1}$, θ is the real number and ξ is the amplitude factor. Now, substituting Eq. (24) into the homogeneous part of Eq. (18) gives:

$$E_m^{n+1}\xi^{n+1}e^{i(\mathrm{m}-1)\theta} - F_m^{n+1}\xi^{n+1}e^{i\,\mathrm{m}\theta} + G_m^{n+1}\xi^{n+1}e^{i(\mathrm{m}+1)\theta}$$
$$= -\varepsilon\frac{\xi^n e^{i(\mathrm{m}+1)\theta} - 2\xi^n e^{i\,\mathrm{m}\theta} + \xi^n e^{i(\mathrm{m}-1)\theta}}{h^2} - \mu a_m^n \frac{\xi^n e^{i(\mathrm{m}+1)\theta} - \xi^n e^{i(\mathrm{m}-1)\theta}}{2h} + \left(b_m^n - \frac{2}{k}\right)\xi^n e^{i\,\mathrm{m}\theta}$$

This implies that $\xi = \dfrac{-2\varepsilon\left(e^{i\theta} - 2 + e^{-i\theta}\right) - \mu h a_m^n\left(e^{i\theta} - e^{-i\theta}\right) + 2h^2 b_m^n}{2\varepsilon\sigma\left(e^{i\theta} + e^{-i\theta} - 2\right) + \mu h a_m^{n+1}\left(e^{i\theta} - e^{-i\theta}\right) - 2h^2 b_m^{n+1}}$

For sufficiently small mesh size *h*, we have the amplitude factor $\xi = \dfrac{-1}{\sigma}$ and the condition to be stable is $|\xi| \le 1$ leads to: $|\xi| = \left|\dfrac{-1}{\sigma}\right| = \left|-\dfrac{2}{\alpha\rho}\tanh\left(\dfrac{\alpha\rho}{2}\right)\right| \le 1$ which yields $-\dfrac{\alpha\rho}{2} \le \tanh\left(\dfrac{\alpha\rho}{2}\right) \le \dfrac{\alpha\rho}{2}$

Since, $\rho = \dfrac{\mu h}{\varepsilon}$ as $h \to 0$, $\tanh\left(\dfrac{\alpha\rho}{2}\right) \to 0$. Therefore, $|\xi| \le 1$.

Hence, the developed scheme in Eq. (18) is stable for any value of mesh sizes. Thus, the developed scheme in Eq. (18) is unconditionally stable by Lax Richtmyer definition [10, 13].

To investigate the consistency of the method, we have considered before extrapolation Eq. (19) and after extrapolation Eq. (23), and then truncation terms vanish as $h \to 0$ and $k \to 0$. Hence, the scheme is consistent with the orders of $O\left(h^2 + k^2\right)$ and $O\left(h^4 + k^4\right)$ respectively. Therefore, the constructed scheme is convergent by Lax's equivalence theorem, as stated in books by Smith [12] and Zhilin et. al. [13].

5. Numerical Results and discussions

Since the exact solution for such type of problems is not available, the maximum absolute errors at all the mesh points are evaluated for before and after extrapolation using the formula

$E_{\varepsilon,\mu}^{M,N} = \max\limits_{0\le m\le M;\ 0\le n\le N}\left|u_m^n - u_{2m}^{2n}\right|$ and $E_{\varepsilon,\mu}^{M,N} = \max\limits_{0\le m\le M;\ 0\le n\le N}\left|\left(u_m^n\right)^{ext} - \left(u_{2m}^{2n}\right)^{ext}\right|$ respectively.

where u_m^n is approximate solution obtained using a constant space mash size *h* and time step *k* and u_{2m}^{2n} is also approximate solution produced using space and time step $\frac{h}{2}$, $\frac{k}{2}$. Also, its solutions obtained by Richardson extrapolation are $\left(u_m^n\right)^{ext}$ and $\left(u_{2m}^{2n}\right)^{ext}$. Likewise, we compute the numerical rates of convergence as $R = \dfrac{\log E_{\varepsilon,\mu}^{M,N} - \log E_{\varepsilon,\mu}^{2M,2N}}{\log 2}$

Example 1: Consider the problem

$$\varepsilon\frac{\partial^2 u}{\partial x^2}+\mu(1+x)\frac{\partial u}{\partial x}-u(x,t)=\frac{\partial u}{\partial t}+16x^2\left(1-x\right)^2,\ (x,t)\in\Omega:=(0,1)\times(0,T]$$

subject to the conditions: $u(x,0)=0,\ \ x\in[0,1]$ and $u(0,t)=0=u(1,t),\ \ t\in[0,T]$
For this example, the obtained numerical results given below in Tables 1 – 3 and Figure 1.

Example 2: This example corresponds to the following IBVP

$$\varepsilon\frac{\partial^2 u}{\partial x^2}+\mu(1+x(1-x)+t^2)\frac{\partial u}{\partial x}-(1+5xt)u(x,t)=\frac{\partial u}{\partial t}+x(1-x)(e^t-1)$$

subject to the conditions: $u(x,0)=0,\ \ x\in[0,1]$ and $u(0,t)=0=u(1,t),\ \ t\in[0,1]$. And numerical results given below in Tables 4 and 5 with Figure 1.

Table 1. Comparison maximum absolute errors for Example 1 at $M=32,\ k=\dfrac{0.125}{4}$

$\mu\downarrow\ \varepsilon\rightarrow$	10^{-2}	10^{-4}	10^{-6}	10^{-8}
Present Method				
10^{-2}	1.3131e-06	2.2236e-07	2.6487e-06	2.6521e-06
10^{-4}	1.2750e-06	2.5782e-08	4.9088e-10	2.4534e-08
10^{-8}	1.2746e-06	2.4962e-08	2.9731e-10	2.9926e-10
10^{-10}	1.2746e-06	2.4954e-08	2.9747e-10	2.9757e-10
Results in [2]				
10^{-2}	1.7212e-02	1.7507e-02	2.2799e-02	2.2801e-02
10^{-4}	1.7000e-02	1.6928e-02	1.6913e-02	1.6962e-02
10^{-8}	1.6998e-02	1.6923e-02	1.6908e-02	1.6917e-02
10^{-10}	1.6998e-02	1.6923e-02	1.6908e-02	1.6917e-02

Table 2. Maximum absolute errors and rate of convergence for Example 1 at $\varepsilon=10^{-12},\ T=1$ and $M=N$

$\mu\downarrow\ N\rightarrow$	8	16	32	64	128	256
After extrapolation						
10^{-8}	2.0138e-07	1.2620e-08	8.2113e-10	7.3934e-11	2.6237e-11	1.3436e-11
	3.9961	3.9420	3.4733	1.4946	0.9655	---
10^{-10}	2.0123e-07	1.2548e-08	7.8380e-10	4.8977e-11	3.0789e-12	2.0339e-13
	4.0033	4.0008	4.0003	3.9916	3.9201	---
10^{-12}	2.0123e-07	1.2548e-08	7.8377e-10	4.8983e-11	3.0536e-12	2.2882e-13
	4.0033					

		4.0009	4.0001	4.0037	3.7382	---
Before extrapolation						
10^{-8}	3.6002e-04	8.9862e-05	2.2456e-05	5.6135e-06	1.4033e-06	3.5082e-07
	2.0023	2.0006	2.0001	2.0001	2.0000	---
10^{-10}	3.6002e-04	8.9862e-05	2.2457e-05	5.6136e-06	1.4034e-06	3.5084e-07
	2.0023	2.0005	2.0002	2.0000	2.0000	---
10^{-12}	3.6002e-04	8.9862e-05	2.2457e-05	5.6136e-06	1.4034e-06	3.5084e-07
	2.0023	2.0005	2.0002	2.0000	2.0000	---

Table 3. Comparison of maximum absolute errors for Example 2 at $\mu = 10^{-7}$

$\varepsilon \downarrow$	$M = 64$	128	256	512
	$N = 16$	32	64	128
Present Method				
10^{-6}	1.7532e-08	1.0945e-09	6.0268e-10	8.3094e-10
10^{-7}	1.7532e-08	1.0945e-09	6.8464e-11	2.6425e-11
10^{-8}	1.7532e-08	1.0945e-09	6.8466e-11	4.2801e-12
10^{-9}	1.7532e-08	1.0945e-09	6.8497e-11	4.2873e-12
Results in [2]				
10^{-6}	3.8754e-5	1.0214e-5	2.6170e-6	6.6241e-7
10^{-7}	3.8753e-5	1.0214e-5	2.6170e-6	6.6241e-7
10^{-8}	3.8753e-5	1.0214e-5	2.6170e-6	6.6241e-7
10^{-9}	3.8753e-5	1.0214e-5	2.5461e-6	6.6241e-7
Results in [1]				
10^{-6}	9.6949e−4	4.9906e−4	2.5231e−4	1.2824e−4
10^{-7}	9.8712e−4	5.0049e−4	2.5485e−4	1.2853e−4
10^{-8}	9.5128e−4	5.0026e−4	2.5237e−4	1.2781e−4
10^{-9}	9.6746e−4	5.0012e−4	2.5461e−4	1.2803e−4

Table 4. Maximum absolute errors for Example 2 at $\varepsilon = 10^{-8}$ and number of intervals $M = N$

$\mu \downarrow N \rightarrow$	8	16	32	64	128	256
After extrapolation						
10^{-8}	2.7269e-07	1.7499e-08	1.0945e-09	6.8442e-11	4.2783e-12	2.6702e-13
10^{-10}	2.7269e-07	1.7499e-08	1.0945e-09	6.8442e-11	4.2782e-12	2.6825e-13
10^{-12}	2.7269e-07	1.7499e-08	1.0945e-09	6.8441e-11	4.2783e-12	2.6698e-13
Before extrapolation						
10^{-8}	1.3949e-04	3.5101e-05	8.7729e-06	2.1959e-06	5.4909e-07	1.3728e-07
10^{-10}	1.3949e-04	3.5101e-05	8.7729e-06	2.1959e-06	5.4909e-07	1.3728e-07
10^{-12}	1.3949e-04	3.5101e-05	8.7729e-06	2.1959e-06	5.4909e-07	1.3728e-07

Table 5. Order of convergence for Example 2 at $\varepsilon = 10^{-8}$ and number of intervals $M = N$

$\mu \downarrow N \rightarrow$	8	16	32	64	128
After extrapolation					
10^{-8}	3.9619	3.9989	3.9992	3.9998	4.0020
10^{-10}	3.9619	3.9989	3.9992	3.9998	3.9954
10^{-12}	3.9619	3.9989	3.9993	3.9998	4.0022
Before extrapolation					
10^{-8}	1.9906	2.0004	1.9982	1.9997	1.9999
10^{-10}	1.9906	2.0004	1.9982	1.9997	1.9999
10^{-12}	1.9906	2.0004	1.9982	1.9997	1.9999

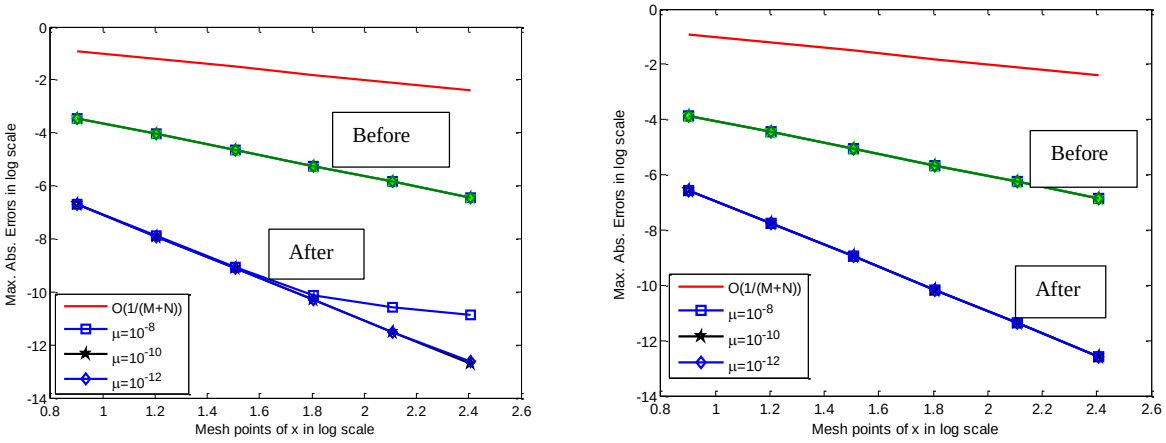

Fig. 1. Log-log plot of maximum absolute errors before and after Richardson extrapolation presented in Table 2 and 4 for Example 1 in the left side and for Example 2 in the right adjacent.

From the results presented in Tables 1 and 3 demonstrates higher order fitted operator finite difference method gives more accurate numerical solution than the existing method. As far results presented in Tables 2, 4 and 5, one can observe that effects of using Richardson extrapolation method to produce more accurate numerical solution corresponding to higher rate of convergence for singularly perturbed parabolic IBVPs with two small positive parameters. Besides, clearly to verify the use of Richardson extrapolation method on numerical scheme to increase accuracy of numerical solution and accelerate order of convergence, one can realize by results confirmed in Figure 1. Moreover, Figure 1 specifies that accuracy of solution increases as number of mesh interval of the domain increases which indicates that convergence of the method.

Conclusion

The key purpose of this work is to formulate and investigate higher order fitted operator finite difference method to solve singularly perturbed parabolic convection-diffusion IBVPs with two small positive parameters. We first discretize the solution domain in the time direction only which leads to ordinary differential equation with respect to space variable. Secondly, full discretization of domain, derivatives in the differential equations are replaced by central finite difference

approximation, introduce and determine the value of fitting parameter on $(n+1)^{th}$ - time level and then the obtained finite difference approximation yields on two-level time direction and three-term recurrence relations in spatial derivatives that can be solved by tri-diagonal solver. Thirdly, applying Richardson extrapolation method to accelerate its rate of convergence from second order to fourth order convergent. Consistency and stability of proposed method have been established very well to guarantee the convergence of the method. Finally, it is validated by considering test examples and displaying numerical results to care the theoretical results and to determine the effectiveness of using the present method. Overall, the developed method is consistent, stable and produces more accurate numerical solution than the existing one for solving singularly perturbed parabolic initial boundary value problems with two small positive parameters.

References

[1]. Das P. and Mehrmann V., Numerical solution of singularly perturbed convection-diffusion-reaction problems with two small parameters, BIT Numer Math, DOI 10.1007/s10543-015-0559-8, 2015.

[2]. Gupta V., Kadalbajoo M. K. and Dubey R. K., A parameter uniform higher order finite difference scheme for singularly perturbed time-dependent parabolic problem with two small parameters, International Journal of Computer Mathematics, DOI: 10.1080/00207160.2018.1432856, 2018.

[3]. Jha A. and Kadalbajoo M. K., A robust layer adapted difference method for singularly perturbed two-parameter parabolic problems**,** International Journal of Computer Mathematics, Taylor and Frances group, 92 1204–1221, 2015.

[4]. Kadalbajoo M. K. and Yadaw A.S., Parameter-uniform finite element method for two-parameter singularly perturbed parabolic reaction-diffusion problems, Int. J. Comput. Methods, 9**,** 1250047-1 - 1250047-16, 2012.

[5]. Kumar V. and Srinivasan B., A novel adaptive mesh strategy for singularly perturbed parabolic convection diffusion problems, Differ Equ Dyn Syst, DOI 10.1007/s12591-017-0394-2, 2017.

[6]. Miller H. J.J, O'Riordan E. and Shishkin I. G., Fitted numerical methods for singular perturbation problems, Error estimate in the maximum norm for linear problems in one and two dimensions, World Scientific, 1996.

[7]. Morton K. W., Numerical solution of convection-diffusion problems, CRC Press, Taylor and Francis group, 1996.

[8]. Munyakazi J. B., A Robust Finite Difference Method for Two-Parameter Parabolic Convection-Diffusion Problems, An International Journal of Applied Mathematics & Information Sciences, 9, 2877-2883, 2015.

[9]. Roos G. H., Stynes M.and Tobiska L., Robust numerical methods for singularly perturbed differential equations, Convection-Diffusion-Reaction and Flow Problems, Springer Series in Computational Mathematics, 2008.

[10]. Smith G. D., Numerical solution of partial differential equations, Finite difference methods, Third edition, Oxford University Pres, 1985.

[11]. Suayip Y. and S. Niyazi S., Numerical solutions of singularly perturbed one-dimensional parabolic convection–diffusion problems by the Bessel collocation method, Applied Mathematics and Computation, 220, 305–315, 2013.

[12]. Zahra W. K., El-Azab M. S. and El Mhlawy A. M. (2014)**,** Spline difference scheme for two-parameter singularly perturbed partial differential **e**quations, J. Appl. Math. and Informatics, 32**,** 185 – 201, 2014.

[13]. Zhilin L., Qiao Z. and Tang T. Numerical solution of differential equations, Introduction to finite difference and finite element methods, printed in the United Kingdom by Clays, 2018.

International Journal of Engineering & Applied Sciences (IJEAS)
Vol.11, Issue 4 (2019) 468-475
http://dx.doi.org/10.24107/ijeas.646718
Int J Eng Appl Sci 11(4) (2019) 468-475

Finite Element Modeling of Receding Contact Problem

Murat Yaylacı [a], Mehmet Çağrı Bayrak [b], Mehmet Avcar [c]*

[a,] *Recep Tayyip Erdogan University, Department of Civil Engineering, 53100, Rize, Turkey*
[b,c,] *Suleyman Demirel University, Department of Civil Engineering, 3220, Isparta, Turkey*
[*] *E-mail address*: murat.yaylaci@erdogan.edu.tr [a], mcbayrak@yahoo.com [b], mehmetavcar@yahoo.com [c]

ORCID numbers of authors:
0000-0003-0407-1685[a], 0000-0002-9995-7325[b], 0000-0002-0689-0601[c]

Received date: 14.11.2019
Accepted date: 26.11.2019

Abstract

In this study, the contact problem of an elastic layer resting on the rigid foundation is examined. For this aim, two-dimensional analysis has been performed using Finite Element Method (FEM) based software called ANSYS. In the solution of the problem, the mass forces of the layers are neglected and the thickness through z-axis direction is taken as a unit since the problem is examined for the plane state. The contact length between the punch and layer and the resulting contact stresses are obtained for various dimensionless parameters.

Keywords: Contact Mechanics, Plane contact problem, FEM analysis

1. Introduction

Contact problems have found wide application areas in engineering structures of practical importance. Foundations, road and airport superstructures, railways, fuel tanks, grain silos, cylindrical shafts and marbles are some of examples of these applications. Therefore, contact problems attracted the attentions of many scientists, and so open literature includes numerous analytical and numerical studies on contact problems. Hertz [1] presented an analytical solution for the contact problem of two elastic bodies with curved surfaces. Weitsman [2] reported an approximate solution for the radius of contact between an elastic plate and a semi-infinite elastic half space. Keer et al. [3] considered the smooth receding contact between an elastic layer and a half space when the two bodies arc pressed together. Ratwani and Erdogan [4] examined the plane contact problem for an elastic layer lying on an elastic half space. Nowell and Hills [5] studied the plane elastic contact between a thin strip and symmetric rollers. Chan and Tuba [6] described modified finite element method for solving problems of elastic bodies in contact. Francavilla and Zienkiewicz [7] proposed a simple procedure of obtaining flexibility matrices in terms of contact pressures at possible contact points of two bodies allows the frictionless

contact pressures to be solved as a quasi-linear problem. Jing and Liao [8] examined an improved finite element scheme for elastic contact problems with friction is improved by introducing the concept of a contact node pair. Garrido et al. [9] applied boundary element method to the receding contact problems with friction. Garrido and Lorenzana [10] presented a new algorithm for the boundary element analysis of the two-dimensional contact problem between elastic solids involving large displacements. Yaylacı et al. [11] dealt with the numerical analysis of the symmetric contact problem of two bonded layers resting on an elastic half plane compressed with a rigid punch using FEM based ANSYS and ABAQUS software.

In the present paper, two-dimensional analysis is performed using Finite Element Method (FEM) based software called ANSYS [12] for the contact problem of an elastic layer resting on the rigid foundation subjected to the concentrated load by a rigid punch. Several analyses are conducted for determining the contact length between the punch and layer and the resulting contact stresses for versus dimensionless parameters.

2. The Analysis of the Problem

Figure 1 shows the geometry of frictionless contact problem of the rigidly supported elastic layer, where h is the height of the elastic layer and the concentrated load is applied via a rigid punch with the radius R to the upper surface of the elastic layer. The layer is in contact with punch in the interval (-a, +a) and extends along the x axis in the range (-∞, + ∞). Since the problem is symmetrical with respect to the y axis, the calculations are made in the range (0, + ∞). In the solution of the problem, the thickness is taken as a unit since the problem is examined for the plane state, as well as the mass forces and friction are neglected in the solution of the problem.

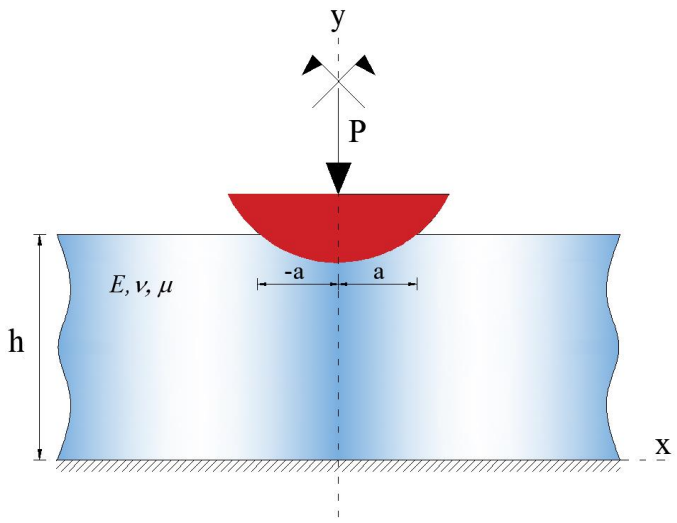

Fig. 1. The geometry of the problem

Here, μ, ν and *E* denote the shear modulus, Poisson's ratio, and Young's modulus of the layer, respectively.

Figure 2 shows the geometry of finite element analysis. The problem is modeled symmetrically with respect to the y axis and the weight of the layer is neglected in here. Linear, elastic and isotropic materials are used in all parts of the finite element model. In the analyzes, the half-length and height of the layer taken to be L = 1 m and h = 0.1m, respectively.

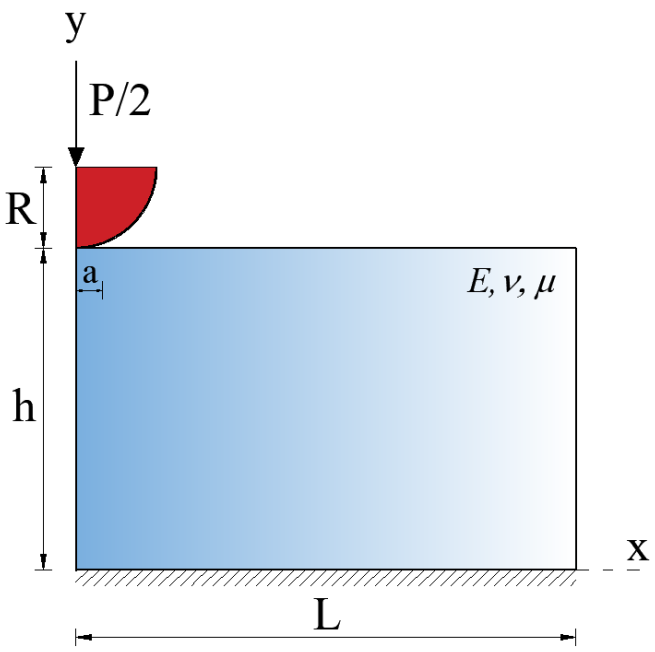

Fig. 2. The geometry of the analysis

Figure 3 shows the geometry of ANSYS. The element choice is especially important in determining the mathematical model to be used in the analysis. The elements are selected according to the type of analysis to be performed. Distinct types of elements may be used for static, thermal, fluid, or electromagnetic analyses. Similarly, whether the model to be analyzed is two or three dimensional is another significant factor in the element choice. Furthermore, the type and number of degrees of freedom of the joints of selected element are essential for the exact analysis. In the analysis, PLANE183 type structural element of the ANSYS package library is used. The PLANE183 type element is defined by eight joints and each joint has two degrees of freedom and no rotation as well as it has plasticity, withstands large flexes, and has a great deal of deformation.

Fig. 3. The geometry of ANSYS

Figure 4 shows the contact pair of ANSYS. The surface-to-surface contact model is used to model the contact pair. Contact pairs consist of two element types, i.e., TARGET and CONTACT element types. The target surface TARGE169 and the contact surface CONTA172 with three joints are used to form the contact pair.

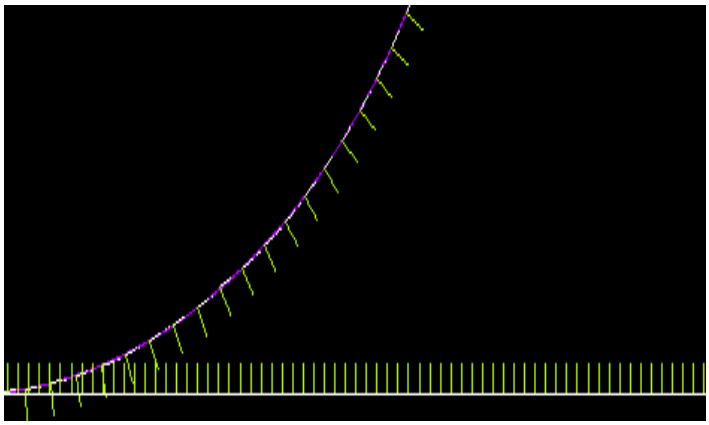

Fig. 4. The contact pair of ANSYS

Figure 5 shows the mesh of the present model. Here, the material properties and element types of the parts in the geometry are assigned mesh structure and size are determined. After the application of the boundary conditions and loading, the problem is solved with the help of the ANSYS program. 4155 joint points and 1450 elements are used to solve the present problem. The deformed shapes of the model are given in Figure 6.

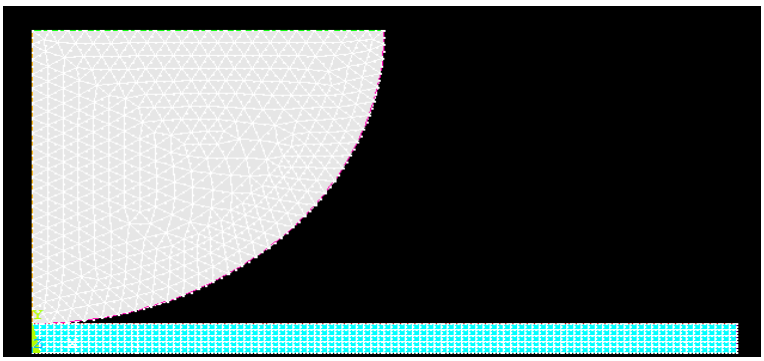

Fig. 5. The mesh of model

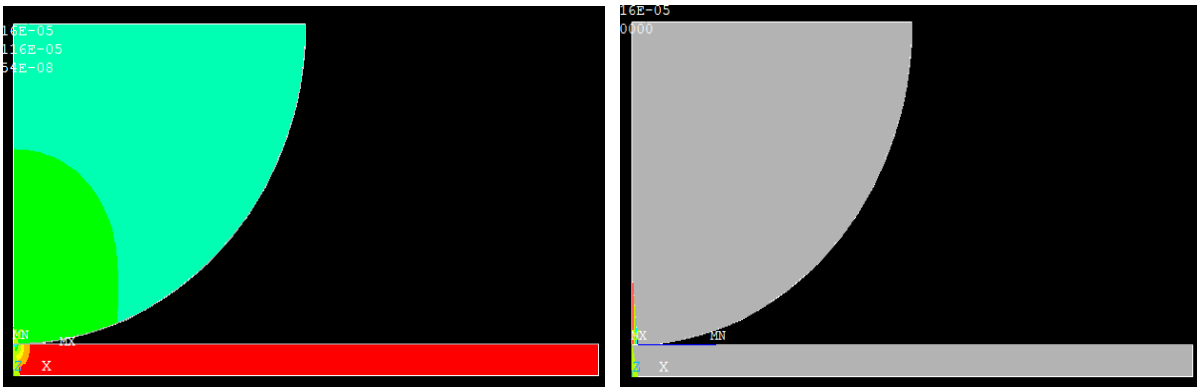

Fig. 6. The deformed shapes of the model

3. The Numerical Results

Figure 7 shows the variation of contact length between the elastic layer and the rigid punch, (a/h), versus the punch radius and load ratio. Here, the variation of the load is expressed with the dimensionless ratio $\mu/(P/h)$. It is found that the contact distances decrease with the increase of the ratio $\mu_0/(P/h)$. Besides, the contact length increases with the increase of the punch radius.

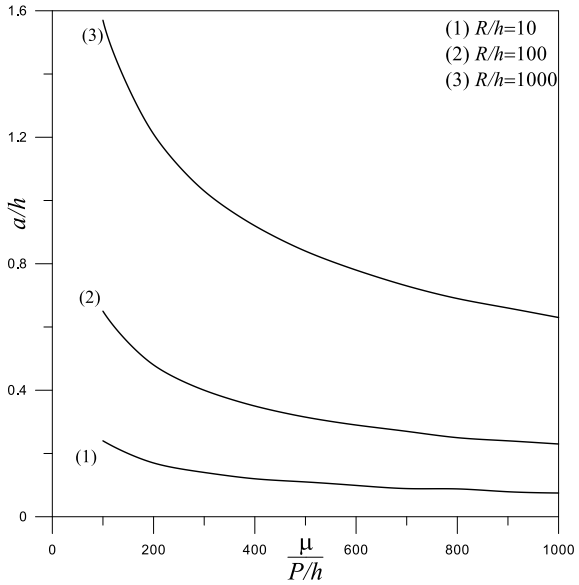

Fig. 7. The variation of the contact length versus the punch radius and load ratio (ν=0.25)

Figure 8 shows the variation of the contact length versus punch radius and Poisson's ratio, ν. It is seen that as Poisson's ratio increases, the contact length decreases, since the body becomes more rigid. Besides, the contact length increases with the increase of the punch radius.

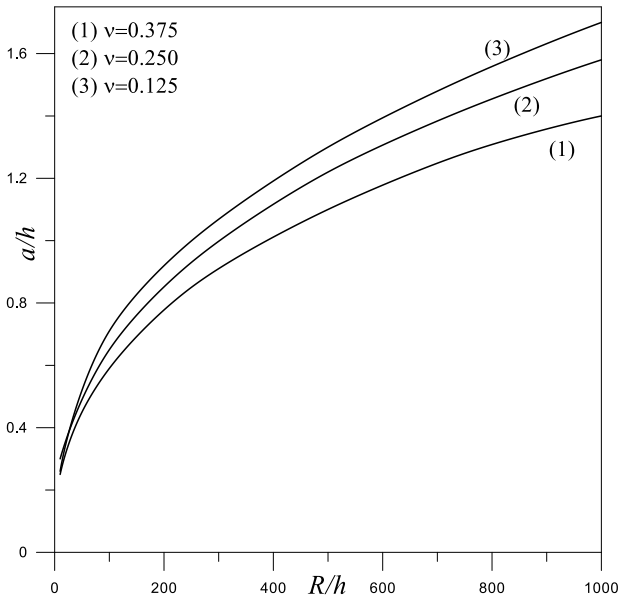

Fig. 8. The variation of the contact length versus the punch radius and Possions's ratio $\left(\frac{\mu}{P/h} = 100\right)$

Figure 9 shows the variation of dimensionless contact stress versus load ratios. It is concluded that as the load ratio increases, the dimensionless contact stresses under the punch increase because the decrease of half contact length.

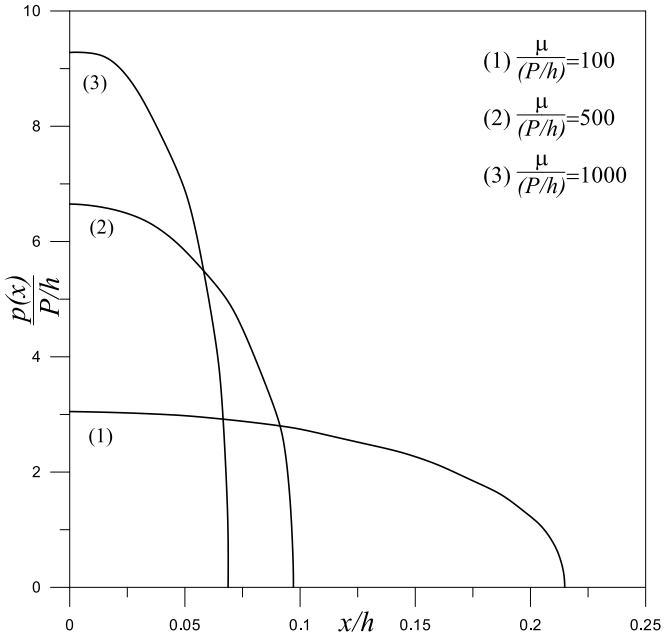

Fig. 9. The variation of dimensionless contact stress versus of load ratios *(ν=0.25, R/h=10)*

Figure 10 shows the variation of the dimensionless contact stress versus punch radius. It is observed that as the block radius increases, the maximum value of the dimensionless contact stress under the punch decreases.

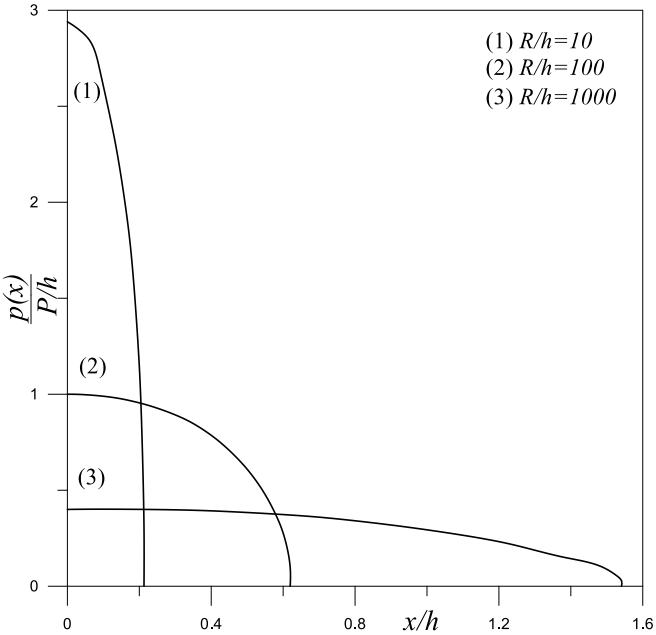

Fig. 10. The variation of the dimensionless contact stress versus punch radius *(ν=0.25,* $\frac{\mu}{P/h} = 100$*)*

Figure 11 shows the variation of the dimensionless contact stress versus Possion's ratio. It is found that as the value of Poisson's ratio decreases, the contact length increases and thus the load spreads over a larger area and the contact stresses decrease.

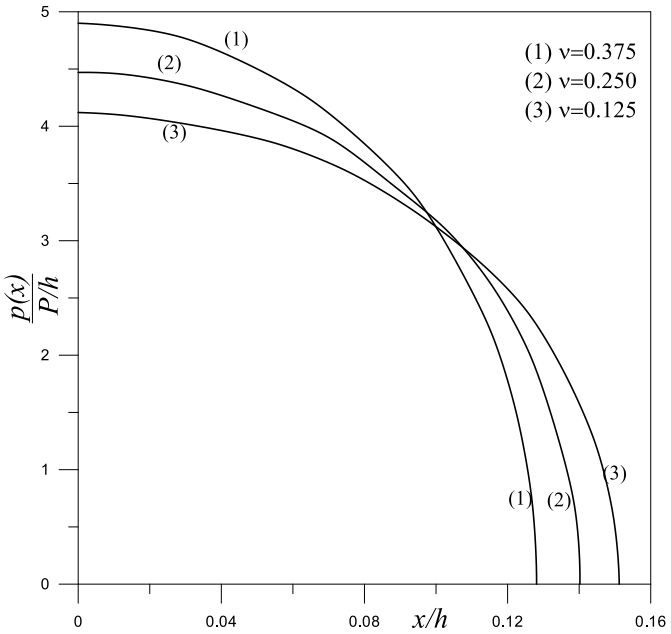

Fig. 11. The variation of the dimensionless contact stress versus Poisson's ratio *(R/h=10,* $\frac{\mu}{P/h} = 100$*)*

4. Conclusions

In this study, contact problem of an elastic layer resting on the rigid foundation is examined using Finite Element Method (FEM) based software called ANSYS. The contact length between the punch and layer and the resulting contact stresses are obtained for various dimensionless parameters

Here, the following results are gotten

a) The contact distances decrease with the increase of the load ratio
b) The contact length increases with the increase of the punch radius
c) The dimensionless contact stresses under the punch increase with the increase of load ratio
d) The maximum value of the dimensionless contact stress decreases with the increase of the block radius
e) The contact stresses decrease with the decrease of the value of Poisson's ratio

References

[1] Hertz, H., Ueber die Berührung fester elastischer Körper, *Journal Fur Die Reine Und Angewandte Mathematik*, 1882, 156–71, 1882. doi:10.1515/crll.1882.92.156

[2] Weitsman, Y., On the unbonded contact between plates and an elastic half space, *Journal of Applied Mechanics, Transactions ASME*, 1964. doi:10.1115/1.3564607

[3] Keer, L.M., Dundurs, J., Tsai, K.C., Problems involving a receding contact between a layer and a half space, *Journal of Applied Mechanics, Transactions ASME*, 1972. doi:10.1115/1.3422839

[4] Ratwani, M., Erdogan, F., On the plane contact problem for a frictionless elastic layer, *International Journal of Solids and Structures*, 1973. doi:10.1016/0020-7683(73)90021-8

[5] Nowell, D., Hills, D.A., Contact problems incorporating elastic layers, *International Journal of Solids and Structures*, 1988. doi:10.1016/0020-7683(88)90102-3

[6] Chan, S.K., Tuba, I.S., A finite element method for contact problems of solid bodies-Part I. Theory and validation, *International Journal of Mechanical Sciences*, 13, 615–25, 1971. doi:10.1016/0020-7403(71)90032-4

[7] Francavilla, A., Zienkiewicz, O.C., A note on numerical computation of elastic contact problems, *International Journal for Numerical Methods in Engineering*, 9, 913–24, 1975. doi:10.1002/nme.1620090410

[8] Jing, H.S., Liao, M.L., An improved finite element scheme for elastic contact problems with friction, *Computers and Structures*, 35, 571–8, 1990. doi:10.1016/0045-7949(90)90385-F

[9] Garrido, J.A., Foces, A., Paris, F., B.E.M. applied to receding contact problems with friction, *Mathematical and Computer Modelling*, 15, 143–53, 1991. doi:10.1016/0895-7177(91)90060-K

[10] Garrido, J.A., Lorenzana, A., Receding contact problem involving large displacements using the BEM, *Engineering Analysis with Boundary Elements*, 21, 295–303, 1998. doi:10.1016/s0955-7997(98)00018-6

[11] Yaylaci, M., Terzi, C., Avcar, M., Numerical analysis of the receding contact problem of two bonded layers resting on an elastic half plane, *Structural Engineering and Mechanics*, accepted, 2019

[12] ANSYS, Swanson Analysis Systems Inc. Houston PA, USA., 2013

International Journal of Engineering & Applied Sciences (IJEAS)
Vol.11, Issue 4 (2019) 476-493
http://dx.doi.org/10.24107/ijeas.647640
Int J Eng Appl Sci 11(4) (2019) 476-493

Exponentially Fitted Finite Difference Method for Singularly Perturbed Delay Differential Equations with Integral Boundary Condition

Habtamu Garoma Debela [a]*, *Gemechis File Duressa* [b]

[a,b]*Department of Mathematics, Jimma University, Jimma, P. O. Box 378, ETHIOPIA*

E-mail address: habte200@gmail.com [a*], gammeef@gmail.com [b]

ORCID numbers of authors:
0000-0003-0109-6860[a], 0000-0003-1889-4690[b]

Received date: 16.11.2019
Accepted date: 28.11.2019

Abstract

In this paper, exponentially fitted finite difference method for solving singularly perturbed delay differential equation with integral boundary condition is considered. To treat the integral boundary condition, Simpson's rule is applied. The stability and parameter uniform convergence of the proposed method are proved. To validate the applicability of the scheme, two model problems are considered for numerical experimentation and solved for different values of the perturbation parameter, ε and mesh size, h. The numerical results are tabulated in terms of maximum absolute errors and rate of convergence and it is observed that the present method is more accurate and ε-uniformly convergent for $h \geq \varepsilon$ where the classical numerical methods fails to give good result and it also improves the results of the methods existing in the literature.

Keywords: Singularly perturbed problems, Delay differential equation, Exponentially fitted operator, Integral boundary condition

Mathematics Subject Classification: 65L11 · 65L12 · 65L20

1. Introduction

A differential equation is said to be singularly perturbed delay differential equation, if it includes at least one delay term, involving unknown functions occurring with different arguments and also the highest derivative term is multiplied by a small parameter. Such type of delay differential equations play very important role in the mathematical modeling of various practical phenomena

and also widely applicable in the fields such as biosciences, control theory, economics, material science, medicine, robotics etc [1-4]. Any system involving a feedback control almost involves time delay. The delay occurs because a finite time is required to sense the information and then react to it.

Finding the solution of singularly perturbed delay differential equations is a challenging problem. In response to these, in recent years there has been a growing interest in numerical methods on singularly perturbed delay differential equations. In mid-eighties to mid-nineties, Lange and Miura [5] studied a class of boundary-value problems for second-order differential-difference equations in which the highest-order derivative is multiplied by a small parameter and proposed some asymptotic method to approximate the solution of this class of differential equations. In 2002, Kadalbajoo and Sharma initiated the numerical study of such type of boundary value problems [6-12]. In [13], a fitted operator scheme on a uniform mesh is suggested to solve an initial value problem for a class of linear and semi linear first order delay differential equations. Amiraliyev and Cimen [14] proposed a first order uniform convergent fitted finite difference scheme for singularly perturbed boundary value problem for a linear second order delay differential equation with large delay in reaction term. Subburayan and Ramanujam [15] gave an initial value technique to solve singularly perturbed boundary value problem for second order delay differential equation of convection-diffusion problem with large delay.

The standard numerical methods used for solving singularly perturbed differential equation are sometime ill posed and fail to give analytical solution when the perturbation parameter ε is small. Therefore, it is necessary to develop suitable numerical methods which are uniformly convergent to solve this type of differential equations.

In the present paper, motivated by the works of [16], we developed exponentially fitted operator finite difference scheme on uniform mesh for the numerical solution of second order singularly perturbed convection-diffusion equations with delay and integral boundary condition.

Throughout our analysis C is generic positive constant that is independent of the parameter ε and number of mesh points $2N$. We assume that $\bar{\Omega}=[0,2]$, $\Omega=(0,2)$, $\Omega_1=(0,1)$, $\Omega_2=(1,2)$. Further, $\Omega^*=\Omega_1\cup\Omega_2$, $\bar{\Omega}^{2N}$ is denoted by $\{0,1,2,...,2N\}$, $\bar{\Omega}_1^{2N}$ is denoted by $\{1,2,...,N-1\}$, Ω_2^{2N} is denoted by $\{N+1,N+2,...,2N-1\}$.

Therefore, the main objective of this study is to develop more accurate, stable and convergent exponentially fitted operator finite difference method for solving singularly perturbed convection-diffusion problems with integral boundary condition.

2. Statement of the problem

Consider the following singularly perturbed problem

$$Ly(x)=-\varepsilon y''(x)+a(x)y'(x)+b(x)y(x)+c(x)y(x-1)=f(x),\quad x\in\Omega=(0,2) \tag{1}$$

$$y(x)=\phi(x),\quad x\in[-1,0], \tag{2}$$

$$Ky(2)=y(2)-\varepsilon\int_0^2 g(x)y(x)dx=l, \tag{3}$$

where $\phi(x)$ is sufficiently smooth on $[-1,0]$.

For all $x \in \Omega$, it is assumed that the sufficient smooth functions $a(x), b(x)$ and $c(x)$ satisfy $a(x) > \alpha_1 > \alpha > 0,\ b(x) \geq \beta \geq 0,\ c(x) \leq \gamma \leq 0,$ and $\alpha + \beta + \gamma > 0.$ Furthermore, $g(x)$ is non-negative and monotonic with $\int_0^2 g(x)dx < 1.$ The above assumptions ensure that $y \in X = C^0(\Omega) \cap C^1(\Omega) \cap C^2(\Omega_1 \cup \Omega_2).$

The Eqs. (1)–(3) is equivalent to

$$Ly(x) = F(x) \tag{4}$$

Where

$$Ly(x) = \begin{cases} L_1 y(x) = -\varepsilon y''(x) + a(x)y'(x) + b(x)y(x), & x \in \Omega_1 = (0,1) \\ L_2 y(x) = -\varepsilon y''(x) + a(x)y'(x) + b(x)y(x) + c(x)y(x-1), & x \in \Omega_2 = (1,2) \end{cases} \tag{5}$$

$$F(x) = \begin{cases} f(x) - c(x)\phi(x-1), & x \in \Omega_1 \\ f(x), & x \in \Omega_2 \end{cases} \tag{6}$$

with boundary conditions

$$\left.\begin{aligned} & y(x) = \phi(x),\ x \in [-1,0], \\ & y(1^-) = y(1^+),\ \ y'(1^-) = y'(1^+), \\ & Ky(2) = y(2) - \varepsilon \int_0^2 g(x)y(x)dx = l, \end{aligned}\right\} \tag{7}$$

3. Properties of continuous solution

Lemma 3.1: (Maximum Principle) Let $\psi(x)$ be any function in X such that $\psi(0) \geq 0,\ K\psi(2) \geq 0,\ L_1\psi(x) \geq 0, \forall x \in \Omega_1, L_2\psi(x) \geq 0, \forall x \in \Omega_2,$ and $[\psi'](1) \leq 0$ then $\psi(x) \geq 0,\ \forall x \in \bar{\Omega}.$

Proof: Define the test function

$$s(x) = \begin{cases} \dfrac{1}{8} + \dfrac{x}{2}, & x \in [0,1] \\ \dfrac{3}{8} + \dfrac{x}{4}, & x \in [1,2] \end{cases} \tag{8}$$

Note that $s(x) > 0,\ \forall x \in \bar{\Omega},\ Ls(x) > 0,\ \forall x \in \Omega_1 \cup \Omega_2, s(0) > 0,\ Ks(2) > 0$ and $[s'](1) < 0.$

Let $\mu = \max\left\{\frac{-\psi(x)}{s(x)} : x \in \bar{\Omega}\right\}$. Then, there exists $x_0 \in \bar{\Omega}$ such that $\psi(x_0) + \mu s(x_0) = 0$ and $\psi(x) + \mu s(x) \geq 0, \ \forall x \in \bar{\Omega}$. Therefore, the function $(\psi + \mu s)$ attains its minimum at $x = x_0$. Suppose the theorem does not hold true, then $\mu > 0$.

Case (i): $x_0 = 0$

$$0 < (\psi + \mu s)(0) = \psi(0) + \mu s(0) = 0, \quad \text{It is a contradiction.}$$

Case (ii): $x_0 \in \Omega_1$

$$0 < L(\psi + \mu s)(x_0) = -\varepsilon(\psi + \mu s)''(x_0) + a(x_0)(\psi + \mu s)'(x_0) + b(x_0)(\psi + \mu s)(x_0) \leq 0$$

It is a contradiction.

Case (iii): $x_0 = 1$

$$0 \leq [(\psi + \mu s)'](1) = [\psi'](1) + \mu[s'](1) < 0, \text{ It is a contradiction.}$$

Case (iv): $x_0 \in \Omega_2$

$$0 < L(\psi + \mu s)(x_0) = -\varepsilon(\psi + \mu s)''(x_0) + a(x_0)(\psi + \mu s)'(x_0) + b(x_0)(\psi + \mu s)(x_0)$$
$$+ c(x_0)(\psi + \mu s)(x_0 - 1) \leq 0, \text{ It is a contradiction.}$$

Case (v): $x_0 = 2$

$$0 \leq K(\psi + \mu s)(2) = (\psi + \mu s)(2) - \varepsilon \int_0^2 g(x)(\psi + \mu s)(x)dx \leq 0, \text{ It is a contradiction.}$$

Hence, the proof of the theorem.

Lemma 3. 2: (Stability Result) The solution $y(x)$ of the problem (1)–(3), satisfies the bound

$$|y(x)| \leq C \max\left\{|y(0)|, |Ky(2)|, \sup_{x \in \Omega^*} |Ly(x)|\right\}, \ x \in \bar{\Omega}$$

Proof: For the proof refer [16]

Lemma 3.3: The bound for derivative of the solution $y(x)$ of the problem (1)-(3) when $x \in \Omega_1 = (0,1)$ is given by

$$\left|y^{(k)}(x)\right| \leq C\left(1 + \varepsilon^{-k} \exp\left(\frac{-\alpha(1 - x_j)}{\varepsilon}\right)\right), \ k = 0 \leq k \leq 4, \ j = 1, 2, ..., N - 1.$$

Proof: For the proof refer [17]

4. Formulation of the numerical scheme

For small values of ε, the boundary value problem (1)–(3) exhibits strong boundary layer at $x = 2$ and interior layer at $x = 1$ (see [16]) and cannot, in general, be solved analytically because of the dependence of $a(x), b(x)$ and $c(x)$ on the spatial coordinate x. We divide the interval $[0, 2]$ into $2N$ equal parts with constant mesh length h. Let $0 = x_0, x_2, ..., x_N = 1, x_{N+1}, x_{N+2}, ..., x_{2N} = 2$ be the mesh points. Then we have $x_i = ih, \ i = 0, 1, 2, ...2N$. If we consider, the interval $x \in (0,1)$ and the coefficients of (1) are evaluated at the midpoint of each interval, then we will obtain the differential equation

$$\begin{cases} -\varepsilon y''(x) + a(x)y'(x) + b(x)y(x) = f(x) - c(x)\phi(x-1), \quad x \in \Omega_1 = (0,1) \\ y_0 = y(0) = \phi(0) \end{cases} \tag{9}$$

Now, the domain $[0,1]$ is discretized into N equal number of subintervals, each of length h. Let $0 = x_0 < x_1 < ... < x_N = 1$ be the points such that $x_i = ih,\ i = 0,1,2,...,N$. For the discretization, we apply a exponentially fitted operator finite difference method (FOFDM).
From (9) we have

$$-\varepsilon y''(x) + a(x)y'(x) + b(x)y(x) = F(x), \quad x \in \Omega_1 = (0,1) \tag{10}$$

where $F(x) = f(x) - c(x)\phi(x-1)$.
To find the numerical solution of (10) we use the theory applied in asymptotic method for solving singularly perturbed BVPs. In the considered case, the boundary layer is in the right side of the domain i.e. near $x = 1$. From the theory of singular perturbations given by O'Malley [18] and using Taylor's series expansion for $a(x)$ about $x = 1$ and restriction to their first terms, we get the asymptotic solution as

$$y(x) = y_0(x) + (\theta - y_0(1))\exp\left(-\frac{a(1)(1-x)}{\varepsilon}\right), \tag{11}$$

where $y_0(x)$ is the solution of the reduced problem (obtained by setting $\varepsilon = 0$) of (10) which is given by

$$a(x)y'(x) + b(x)y(x) = F(x) \text{ with } y_0(0) = \phi(0). \tag{12}$$

Considering h small enough, the discretized form of (11) becomes

$$y(ih) = y_0(ih) + (\theta - y_0(1))\exp\left(-\frac{a(1)(1-ih)}{\varepsilon}\right),$$

which simplifies to

$$y(ih) = y_0(ih) + (\theta - y_0(1))\exp\left(-a(1)\left(\frac{1}{\varepsilon} - i\rho\right)\right), \tag{13}$$

where $\rho = \frac{h}{\varepsilon},\ h = \frac{1}{N}$.
To handle the effect of the perturbation parameter artificial viscosity (exponentially fitting factor $\sigma(\rho)$) is multiplied on the term containing the perturbation parameter as

$$-\varepsilon\sigma(\rho)y''(x) + a(x)y'(x) + b(x)y(x) = F(x), \tag{14}$$

with boundary conditions $y_0(0) = \phi(0)$ and $y(N) = \theta$

where $y(N)$ is evaluated by Runge-Kutta method from the reduced solution of (12).
Next, we consider the difference approximation of Eq. (9) on a uniform grid $\bar{\Omega}^N = \{x_i\}_{i=0}^N$ and denote $h = x_{i+1} - x_i$.
For any mesh function z_i, define the following difference operators

$$D^+ z_i = \frac{z_{i+1} - z_i}{h}, \quad D^- z_i = \frac{z_i - z_{i-1}}{h}, \quad D^0 z_i = \frac{z_{i+1} - z_{i-1}}{2h}, \quad D^+ D^- z_i = \frac{z_{i+1} - 2z_i + z_{i-1}}{h^2}, \tag{15}$$

By applying the central finite difference scheme on Eq. (14) takes the form

$$-\varepsilon\sigma(\rho)(D^+ D^- y(x_i)) + a(x_i)(D^0 y(x_i)) + b(x_i)y(x_i) = F(x_i), \tag{16}$$

with the boundary conditions $y_0(0) = \phi(0)$ and $y(N) = \theta$.
Using operator, Eq. (10) is rewritten as

$$L^h y_i = F_i \tag{17}$$

with the boundary conditions $y_0 = \phi(0)$ and $y_N = \theta$.
where

$$L^h y_i = -\varepsilon\sigma(\rho)\left(\frac{y_{i+1} - 2y_i + y_{i-1}}{h^2}\right) + a(x_i)\left(\frac{y_{i+1} - y_{i-1}}{2h}\right) + b(x_i)y_i = F_i, \tag{18}$$

Multiplying Eq. (18) by h and considering h small and truncating the term $h(F_i - b(x_i)y(x_i))$, results

$$\frac{\sigma(\rho)}{\rho}\left(y_{i-1} - 2y_i + y_{i+1}\right) + \frac{a(x_i)}{2}\left(y_{i-1} - y_{i+1}\right) = 0 \tag{19}$$

Now using Taylor's series for y_{i-1} and y_{i+1} up to first term and substituting the results in Eq. (19) into Eq. (16) and simplifying, the exponential fitting factor is obtained as

$$\sigma(\rho) = \frac{\sigma a(1)}{2}\coth\left(\frac{\sigma a(1)}{2}\right) \tag{20}$$

Assume that $\bar{\Omega}^{2N}$ denote partition of $[0,2]$ into $2N$ subintervals such that $0 = x_0 < x_1 < \ldots < x_N = 1$ and $1 < x_{N+1} < x_{N+2} < \ldots < x_{2N} = 2$ with $x_i = ih,\ h = \frac{2}{2N} = \frac{1}{N},\ i = 0,1,2,\ldots,2N$.
Case 1: Consider Eq. (4) on the domain $\Omega_1 = (0,1)$ which is given by

$$-\varepsilon y''(x) + a(x)y'(x) + b(x)y(x) = f(x) - c(x)\phi(x-1) \tag{21}$$

Hence, the required finite difference scheme becomes

$$\left(\frac{\varepsilon\sigma(\rho)}{h^2}-\frac{a(x_i)}{2h}\right)y_{i-1}+\left(\frac{-2\varepsilon\sigma(\rho)}{h^2}+b(x_i)\right)y_i+\left(\frac{\varepsilon\sigma(\rho)}{h^2}+\frac{a(x_i)}{2h}\right)y_{i+1}=f_i-c_i\phi(x_i-N) \tag{22}$$

for $i=0,1,2,...,N$.

The numerical scheme in Eq. (22) can be written in three term recurrence relation as

$$E_i y_{i-1}+F_i y_i+G_i y_{i+1}=H_i,\quad i=1,2,...,N \tag{23}$$

where $E_i=\frac{-\varepsilon\sigma}{h^2}-\frac{a_i}{2h}$, $F_i=\frac{2\varepsilon\sigma}{h^2}+b_i$, $G_i=\frac{-\varepsilon\sigma}{h^2}+\frac{a_i}{2h}$, $H_i=f_i-c_i\phi(x_i-N)$,

Case 2: Consider Eq. (4) on the domain $\Omega_2=(1,2)$, for right layer in the domain Ω_2 using exponentially fitted finite difference method, which is given by $-\varepsilon\sigma(\rho)\left(\frac{y_{i+1}-2y_i+y_{i-1}}{h^2}\right)+a_i\left(\frac{y_i-y_{i-1}}{h}\right)+b_i y_i+c_i y(x_i-1)+\tau_1=f_i$ Similarly, this equation can be written as

$$c_i y_j+E_i y_{i-1}+F_i y_i+G_i y_{i+1}=H_i,\quad i=N+1,N+2,...,2N-1 \tag{24}$$

where $y_j=y(x_i-1),\quad j=1,2,...,N$, $E_i=\frac{-\varepsilon\sigma}{h^2}-\frac{a_i}{2h}$, $F_i=\frac{2\varepsilon\sigma}{h^2}+b_i$, $G_i=\frac{-\varepsilon\sigma}{h^2}+\frac{a_i}{2h}$, $H_i=f_i$

Case 3: For $i=2N$, the composite Simpson's rule approximates the integral of $g(x)y(x)$ by

$$\int_0^2 g(x)y(x)dx=\frac{h}{3}\left(g(0)y(0)+g(2)y(2)+2\sum_{i=1}^{2N-1}g(x_{2i})y(x_{2i})+4\sum_{i=1}^{2N}g(x_{2i-1})y(x_{2i-1})\right) \tag{25}$$

Substituting Eq. (25) into Eq. (3) gives

$$y(2)-\frac{\varepsilon h}{3}\left(g(0)y(0)+g(2)y(2)+2\sum_{i=1}^{2N-1}g(x_{2i})y(x_{2i})+4\sum_{i=1}^{2N}g(x_{2i-1})y(x_{2i-1})\right)=L$$

Since $y(0)=\phi(0)$, from Eq. (2), this equation can be re-written as

$$-\frac{4\varepsilon h}{3}\sum_{i=1}^{2N}g(x_{2i-1})y(x_{2i-1})-\frac{2\varepsilon h}{3}\sum_{i=1}^{2N-1}g(x_{2i})y(x_{2i})+\left(1-\frac{\varepsilon h}{3}g(2)\right)y(2)=L+\frac{\varepsilon h}{3}g(0)y(0) \tag{26}$$

Therefore, on the whole domain $\bar{\Omega}=[0,2]$, the basic schemes to solve Eqs. (1)-(3) are the schemes given in Eq. (23), Eq. (24) and Eq. (26) together with the local truncation error of τ_1.

5. Convergence analysis

The discrete scheme corresponding to the original Eqs. (1)–(3) is as follows:

For $i = 1, 2, ..., N-1,$

$$L_1^N Y_i = f_i - b_i \phi_{i-N,} \tag{27}$$

For $i = N+1, ..., 2N-1,$

$$L_2^N Y_i = f_i, \tag{28}$$

subject to the boundary conditions:

$$Y_i = \phi_i,\ i = -N, -N+1, ..., 0 \tag{29}$$

$$K^N Y_{2N} = Y_{2N} - \sum_{i=1}^{2N} \frac{g_{i-1} Y_{i-1} + 4 g_i Y_i + g_{i-1} Y_{i-1}}{3} h_i \tag{30}$$

And $D^- Y_N = D^+ Y_N$

Where $L_1^N Y_i = -\varepsilon \delta^2 Y(x_i) + a(x_i) D^0 Y(x_i) + b(x_i) Y(x_i)$

$L_2^N Y_i = -\varepsilon \delta^2 Y(x_i) + a(x_i) D^0 Y(x_i) + b(x_i) Y(x_i) + c(x_i) Y(x_{i-N})$

Lemma 5.1: (Discrete Maximum Principle) Assume that $\sum_{i=1}^{2N} \frac{g_{i-1} + 4 g_i + g_{i-1}}{3} h_i = \rho < 1$ and mesh function $\psi(x_i)$ satisfies $\psi(x_0) \geq 0,$ and $K^N \psi(x_{2N}) \geq 0,$ Then $L_1^N \psi(x_i) \geq 0,\ \forall x_i \in \Omega_1^{2N}, L_2^N \psi(x_i) \geq 0,\ \forall x_i \in \Omega_2^{2N},$ and $D^+(\psi(x_N)) - D^-(\psi(x_N)) \leq 0$ imply that $\psi(x_i) \geq 0,\ \forall x_i \in \bar{\Omega}^{2N}.$

Proof: Define

$$s(x_i) = \begin{cases} \frac{1}{8} + \frac{x_i}{2}, & x_i \in [0,1] \cap \bar{\Omega}^{2N}, \\ \frac{3}{8} + \frac{x_i}{4}, & x_i \in [1,2] \cap \bar{\Omega}^{2N}, \end{cases}$$

Note that $s(x_i) > 0,\ \forall x_i \in \bar{\Omega}^{2N},\ Ls(x_i) > 0,\ \forall x_i \in \bar{\Omega}_1^{2N} \cup \bar{\Omega}_1^{2N}, s(0) > 0,\ Ks(x_{2N}) > 0$ and $[s'](x_N) < 0.$

Let $\mu = \max \left\{ \frac{-\psi(x_i)}{s(x_i)} :\ x_i \in \bar{\Omega}^{2N} \right\}.$ Then there exists $x_k \in \bar{\Omega}^{2N}$ such that $\psi(x_k) + \mu s(x_k) = 0$ and $\psi(x_i) + \mu s(x_i) \geq 0,\ \forall x_i \in \bar{\Omega}^{2N}.$ Therefore, the function $(\psi + \mu s)$ attains its minimum at $x = x_k.$ Suppose the theorem does not hold true, then $\mu > 0.$

Case (i): $x_k = x_0$

$$0 < (\psi + \mu s)(x_0) = 0, \text{ It is a contradiction.}$$

Case (ii): $x_k \in \Omega_1^{2N}$

$$0 < L_1^N(\psi + \mu s)(x_k) \le 0, \quad \text{It is a contradiction.}$$

Case (iii): $x_k = x_N$

$$0 \le [D(\psi + \mu s)'](x_N) < 0, \quad \text{It is a contradiction.}$$

Case (iv): $x_k \in \Omega_2^{2N}$

$$0 < L_2^N(\psi + \mu s)(x_k) \le 0, \quad \text{It is a contradiction.}$$

Case (v): $x_k = x_{2N}$

$$0 < K^N(\psi + \mu s)x_{2N} = (\psi + \mu s)x_{2N} - \sum_{i=1}^{2N} \frac{g_{i-1}(\psi + \mu s)x_{i-1} + 4g_i(\psi + \mu s)x_i + g_{i-1}(\psi + \mu s)x_{i-1}}{3} h_i \le 0$$

It is a contradiction. Hence the proof of the theorem.

Lemma 5.2: Let $\psi(x_i)$ be any mesh function then for $0 \le i \le 2N$,

$$|\psi(x_i)| \le C \max\left\{ |\psi(x_0)|, |K^N \psi(x_{2N})|, \max_{i \in \Omega_1^{2N} \cup \Omega_2^{2N}} |L^N \psi(x_i)| \right\}$$

Proof: For the proof refer [16]

The following theorem shows the parameter uniform convergence of the scheme developed.

Theorem 5.1: Let $y(x_i)$ and y_i be respectively the exact solution of Eqs. (1)-(3) and numerical solutions of Eq. (17). Then for sufficiently large N, the following parameter uniform error estimate holds:

$$\sup_{0<\varepsilon\le 1} \|y(x_i) - y_i\| \le CN^{-2} \tag{31}$$

Proof: Let us consider the local truncation error defined as

$$L^h(y(x_i) - y_i) = -\varepsilon\sigma(\rho)\left(\frac{d^2}{dx^2} - D^+D^-\right)y(x_i) + a(x_i)\left(\frac{d}{dx} - D^0\right)y(x_i) \tag{32}$$

where $\varepsilon\sigma(\rho) = a(1)\frac{N^{-1}}{2}\coth\left(a(1)\frac{N^{-1}}{2\varepsilon}\right)$ since $\frac{N^{-1}}{2\varepsilon}$. In our assumption $\varepsilon \le h = N^{-1}$.

By considering is fixed and taking the limit for $\varepsilon \to 0$, we obtain the following

$$\lim_{\varepsilon\to 0} \varepsilon\sigma(\rho) = \lim_{\varepsilon\to 0} a(1)\frac{N^{-1}}{2}\coth\left(a(1)\frac{N^{-1}}{2\varepsilon}\right) = CN^{-1}$$

From Taylor series expansion, the bound for the difference becomes

$$\begin{cases} \left\| \left(\frac{d^2}{dx^2} - D^+D^-\right)y(x_i) \right\| \le CN^{-3} \left\| \frac{d^4(y(x_i))}{dx^4} \right\| \\ \left\| \left(\frac{d}{dx} - D^0\right)y(x_i) \right\| \le CN^{-2} \left\| \frac{d^3(y(x_i))}{dx^3} \right\| \end{cases}$$

where $\left\| \frac{d^k(y(x_i))}{dx^k} \right\| = \sup_{x_i \in (x_0, x_N)} \left(\frac{d^k y(x_i)}{dx^k} \right)$, $k = 3, 4.$

Now using the bounds and the assumption $\varepsilon \le N^{-1}$, (32) reduces to

$$\begin{aligned}\left\|L^h(y(x_i)-y_i)\right\| &= \left\|-\varepsilon\sigma(\rho)\left(\frac{d^2}{dx^2}-D^+D^-\right)y(x_i)+a(x_i)\left(\frac{d}{dx}-D^0\right)y(x_i)\right\| \\ &\le \left\|-\varepsilon\sigma(\rho)\left(\frac{d^2}{dx^2}-D^+D^-\right)y(x_i)\right\|+\left\|a(x_i)\left(\frac{d}{dx}-D^0\right)y(x_i)\right\| \\ &\le CN^{-3}\left\|\frac{d^4(y(x_i))}{dx^4}\right\|+CN^{-2}\left\|\frac{d^3(y(x_i))}{dx^3}\right\|\end{aligned} \tag{33}$$

Here, the target is to show the scheme convergence independent on the number of mesh points. By using the bounds for the derivatives of the solution in Lemma 3.4, we obtain

$$\begin{aligned}\left\|L^h(y(x_i)-y_i)\right\| &\le CN^{-3}\left\|\frac{d^4(y(x_i))}{dx^4}\right\|+CN^{-2}\left\|\frac{d^3(y(x_i))}{dx^3}\right\| \\ &\le CN^{-3}\left(1+\varepsilon^{-4}\exp\left(\frac{-\alpha(1-x_j)}{\varepsilon}\right)\right)+CN^{-2}\left(1+\varepsilon^{-3}\exp\left(\frac{-\alpha(1-x_j)}{\varepsilon}\right)\right) \\ &\le CN^{-2}\left(1+\varepsilon^{-4}\exp\left(\frac{-\alpha(1-x_j)}{\varepsilon}\right)\right), \text{ since } \varepsilon^{-4}\ge\varepsilon^{-3}\end{aligned} \tag{34}$$

Lemma 5.3: For a fixed mesh and for $\varepsilon \to 0$, it holds

$$\lim_{\varepsilon\to 0}\max_{1\le j\le N-1}\frac{\exp\left(\frac{-\alpha(1-x_j)}{\varepsilon}\right)}{\varepsilon^m}=0, \quad m=1,2,3,... \tag{35}$$

Proof: Refer from [19]
By using Lemma 5.3 into Eq. (34), results to

$$\left\|L^h(y(x_i)-y_i)\right\| \le CN^{-2} \tag{36}$$

Hence, by discrete maximum principle, we obtain

$$\left\|y(x_i)-y_i\right\| \le CN^{-2} \tag{37}$$

Thus, result of Eq. (37) shows Eq. (31). Hence the proof.
Remark: A similar analysis for convergence may be carried out for finite difference scheme (24).

6. Numerical Examples and Results

In this section, four examples are given to illustrate the numerical method discussed above. The exact solutions of the test problems are not known. Therefore, we use the double mesh principle to estimate the error and compute the experiment rate of convergence to the computed solution. For this we put $E_{\varepsilon}^{h} = \max_{0\le i\le 2N} \left| Y_i^N - Y_{2i}^{2N} \right|$ where Y_i^N and Y_{2i}^{2N} are the i^{th} components of the numerical solutions on meshs of N and $2N$, respectively. We compute the uniform error and the rate of convergence as $E^h = \max_{\varepsilon} E_{\varepsilon}^{h}$ and $R^h = \log_2\left(\frac{E^N}{E^{2N}}\right)$. The numerical results are presented for the values of the perturbation parameter $\varepsilon \in \left\{10^{-4}, 10^{-8}, ..., 10^{-20}\right\}$.

Example 1:

$$-\varepsilon y''(x) + 3y'(x) - y(x-1) = 0, \quad x \in (0,1)\bigcup(1,2)$$
$$y(x) = 1, \quad x \in [-1,0]$$
$$y(2) - \varepsilon\int_0^2 \frac{x}{3} y(x)dx = 2$$

Table 1. Maximum absolute errors and rate of convergence for Example 1 at number of mesh points $2N$

ε	$N=32$	$N=64$	$N=128$	$N=256$	$N=512$
10^{-4}	6.8902e-03	3.4587e-03	1.7327e-03	8.6721e-04	4.3382e-04
	0.9943	0.9972	0.9986	0.9993	
10^{-8}	6.8902e-03	3.4587e-03	1.7327e-03	8.6721e-04	4.3382e-04
	0.9943	0.9972	0.9986	0.9993	
10^{-12}	6.8902e-03	3.4587e-03	1.7327e-03	8.6721e-04	4.3382e-04
	0.9943	0.9972	0.9986	0.9993	
10^{-16}	6.8902e-03	3.4587e-03	1.7327e-03	8.6721e-04	4.3382e-04
	0.9943	0.9972	0.9986	0.9993	
10^{-20}	6.8902e-03	3.4587e-03	1.7327e-03	8.6721e-04	4.3382e-04
	0.9943	0.9972	0.9986	0.9993	

Table 2. Comparisons of maximum absolute errors and rate of convergence for Example 1 at number of mesh points $2N$

$\varepsilon \downarrow N \rightarrow$	32	64	128	256	512
Present Method					
2^{-10}	6.8902e-03	3.4587e-03	1.7327e-03	8.6773e-04	4.3760e-04
2^{-11}	6.8902e-03	3.4587e-03	1.7327e-03	8.6721e-04	4.3382e-04
2^{-12}	6.8902e-03	3.4587e-03	1.7327e-03	8.6721e-04	4.3382e-04
2^{-13}	6.8902e-03	3.4587e-03	1.7327e-03	8.6721e-04	4.3382e-04
2^{-14}	6.8902e-03	3.4587e-03	1.7327e-03	8.6721e-04	4.3382e-04
2^{-15}	6.8902e-03	3.4587e-03	1.7327e-03	8.6721e-04	4.3382e-04
2^{-16}	6.8902e-03	3.4587e-03	1.7327e-03	8.6721e-04	4.3382e-04
2^{-17}	6.8902e-03	3.4587e-03	1.7327e-03	8.6721e-04	4.3382e-04
2^{-18}	6.8902e-03	3.4587e-03	1.7327e-03	8.6721e-04	4.3382e-04
2^{-19}	6.8902e-03	3.4587e-03	1.7327e-03	8.6721e-04	4.3382e-04
2^{-20}	6.8902e-03	3.4587e-03	1.7327e-03	8.6721e-04	4.3382e-04
E^h	**6.8902e-03**	**3.4587e-03**	**1.7327e-03**	**8.6721e-04**	**4.3382e-04**
R^h	**0.9943**	**0.9972**	**0.9986**	**0.9993**	
Result in [16]					
2^{-10}	8.7402e−03	4.0726e−03	1.9156e−03	9.1036e−04	4.3976e−04
2^{-11}	9.3259e-03	4.4288e-03	2.1232e-03	1.0265e-03	5.0201e-04
2^{-12}	9.7404e-03	4.6808e-03	2.2700e-03	1.1087e-03	5.4603e-04
2^{-13}	1.0033e-02	4.8591e-03	2.3738e-03	1.1668e-03	5.7716e-04
2^{-14}	1.0241e-02	4.9852e-03	2.4472e-03	1.2079e-03	5.9917e-04
2^{-15}	1.0387e-02	5.0744e-03	2.4991e-03	1.2370e-03	6.1474e-04
2^{-16}	1.0491e-02	5.1374e-03	2.5358e-03	1.2575e-03	6.2574e-04
2^{-17}	1.0564e-02	5.1820e-03	2.5618e-03	1.2720e-03	6.3352e-04
2^{-18}	1.0616e-02	5.2135e-03	2.5801e-03	1.2823e-03	6.3902e-04
2^{-19}	1.0653e-02	5.2358e-03	2.5931e-03	1.2896e-03	6.4292e-04
2^{-20}	1.0679e-02	5.2516e-03	2.6023e-03	1.2947e-03	6.4567e-04
E^h	**1.0679e-02**	**5.2516e-03**	**2.6023e-03**	**1.2947e-03**	**6.4567e-04**
R^h	**1.0240**	**1.0129**	**1.0071**	**1.0038**	

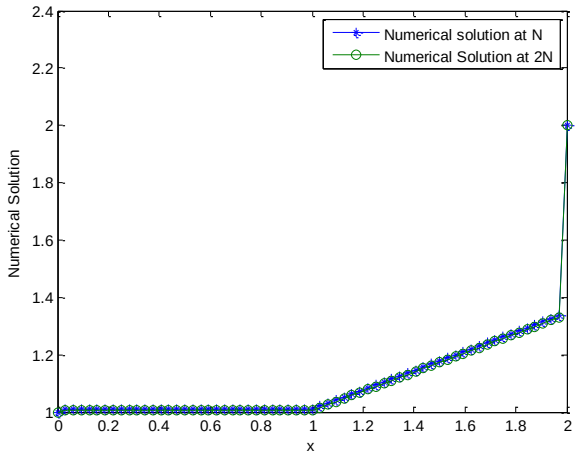

Fig. 1. The behavior of the Numerical Solution for Example 1 at $\varepsilon = 10^{-12}$ and $N = 32$.

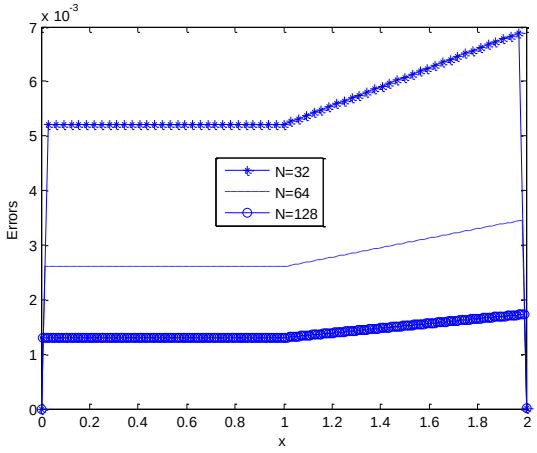

Fig. 2. Point wise absolute error of Example 1 at $\varepsilon = 10^{-12}$ with different mesh size h.

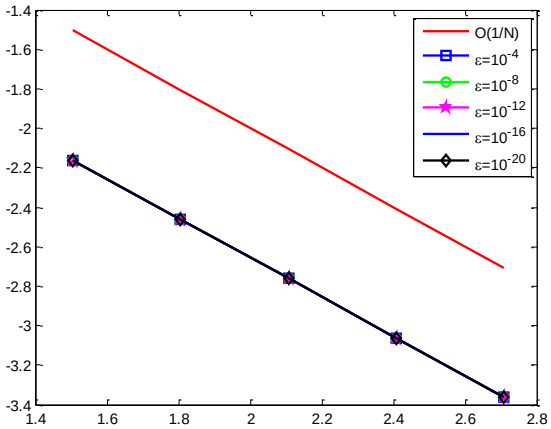

Fig. 3. ε-uniform convergence with NSFDM in Log-Log scale for example 1

Example 2:

$$-\varepsilon y''(x)+(x+10)y'(x)-y(x-1)=x^2, \quad x\in(0,1)\bigcup(1,2)$$
$$y(x)=1, \quad x\in[-1,0]$$
$$y(2)-\varepsilon\int_0^2 \frac{x}{3}y(x)dx=2$$

Table 3. Maximum absolute errors and rate of convergence for Example 2 at number of mesh points $2N$

ε	$N=32$	$N=64$	$N=128$	$N=256$	$N=512$
10^{-4}	1.5579e-03	7.7976e-04	3.9021e-04	1.9520e-04	9.7628e-05
	0.9985	0.9988	0.9993	0.9996	
10^{-8}	1.5579e-03	1.5579e-03	3.9021e-04	1.9520e-04	9.7628e-05
	0.9985	0.9988	0.9993	0.9996	
10^{-12}	1.5579e-03	1.5579e-03	3.9021e-04	1.9520e-04	9.7628e-05
	0.9985	0.9988	0.9993	0.9996	
10^{-16}	1.5579e-03	1.5579e-03	3.9021e-04	1.9520e-04	9.7628e-05
	0.9985	0.9988	0.9993	0.9996	
10^{-20}	1.5579e-03	1.5579e-03	3.9021e-04	1.9520e-04	9.7628e-05
	0.9985	0.9988	0.9993	0.9996	

Table 4. Comparison of Maximum absolute errors and rate of convergence for Example 2 at number of mesh points $2N$

$\varepsilon\downarrow N\rightarrow$	32	64	128	256	512
Present Method					
2^{-10}	1.5579e-03	7.7976e-04	3.9021e-04	1.9520e-04	9.7633e-05
2^{-11}	1.5579e-03	7.7976e-04	3.9021e-04	1.9520e-04	9.7633e-05
2^{-12}	1.5579e-03	7.7976e-04	3.9021e-04	1.9520e-04	9.7633e-05
2^{-13}	1.5579e-03	7.7976e-04	3.9021e-04	1.9520e-04	9.7633e-05
2^{-14}	1.5579e-03	7.7976e-04	3.9021e-04	1.9520e-04	9.7633e-05
2^{-15}	1.5579e-03	7.7976e-04	3.9021e-04	1.9520e-04	9.7633e-05
2^{-16}	1.5579e-03	7.7976e-04	3.9021e-04	1.9520e-04	9.7628e-05
2^{-17}	1.5579e-03	7.7976e-04	3.9021e-04	1.9520e-04	9.7628e-05
2^{-18}	1.5579e-03	7.7976e-04	3.9021e-04	1.9520e-04	9.7628e-05
2^{-19}	1.5579e-03	7.7976e-04	3.9021e-04	1.9520e-04	9.7628e-05
2^{-20}	1.5579e-03	7.7976e-04	3.9021e-04	1.9520e-04	9.7628e-05
E^h	**1.5579e-03**	**7.7976e-04**	**3.9021e-04**	**1.9520e-04**	**9.7628e-05**
R^h	**0.9985**	**0.9988**	**0.9993**	**0.9993**	
Result in [16]					
2^{-10}	5.5958e-03	2.5488e-03	1.1977e-03	5.7296e-04	2.7750e-04
2^{-11}	5.8142e-03	2.6717e-03	1.2671e-03	6.1165e-04	2.9860e-04
2^{-12}	5.9692e-03	2.7588e-03	1.3161e-03	6.3898e-04	3.1349e-04
2^{-13}	6.0790e-03	2.8204e-03	1.3508e-03	6.5829e-04	3.2400e-04

2^{-14}	6.1568e-03	2.8640e-03	1.3753e-03	6.7194e-04	3.3142e-04
2^{-15}	6.2119e-03	2.8948e-03	1.3927e-03	6.8158e-04	3.3667e-04
2^{-16}	6.2509e-03	2.9166e-03	1.4049e-03	6.8840e-04	3.4038e-04
2^{-17}	6.2785e-03	2.9321e-03	1.4136e-03	6.9322e-04	3.4300e-04
2^{-18}	6.2980e-03	2.9430e-03	1.4197e-03	6.9662e-04	3.4485e-04
2^{-19}	6.3118e-03	2.9507e-03	1.4241e-03	6.9903e-04	3.4616e-04
2^{-20}	6.3216e-03	2.9562e-03	1.4271e-03	7.0074e-04	3.4709e-04
E^h	**6.3216e-03**	**2.9562e-03**	**1.4271e-03**	**7.0074e-04**	**3.4709e-04**
R^h	**1.0965**	**1.0505**	**1.0262**	**1.0135**	

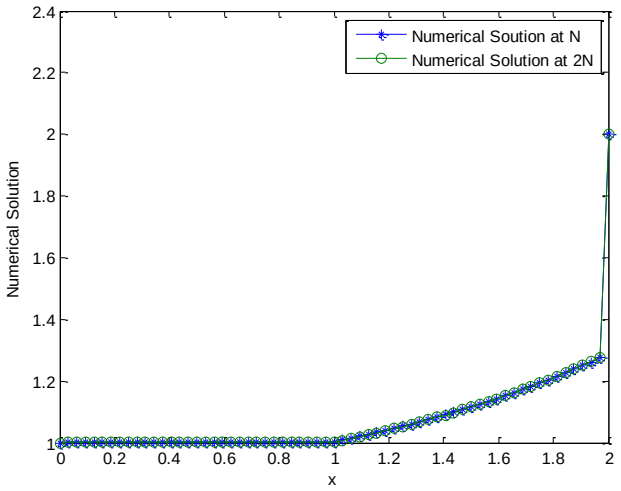

Fig. 4**.** The behavior of numerical solution for example 2 at $\varepsilon = 10^{-12}$ and $N = 32$.

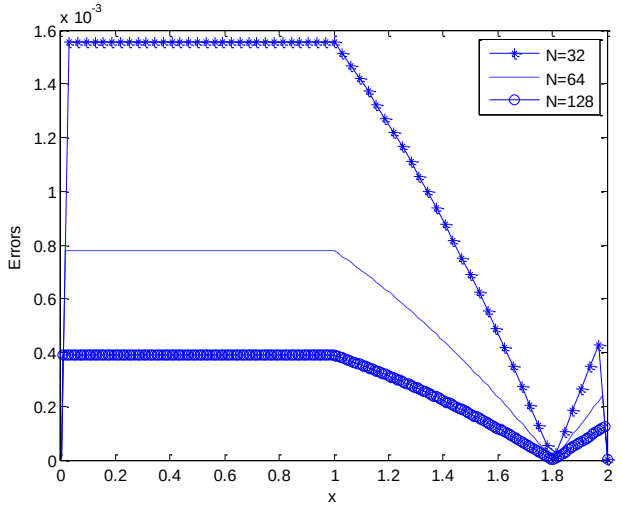

Fig. 5. Point wise absolute error of Example 2 at $\varepsilon = 10^{-12}$ with different mesh size h.

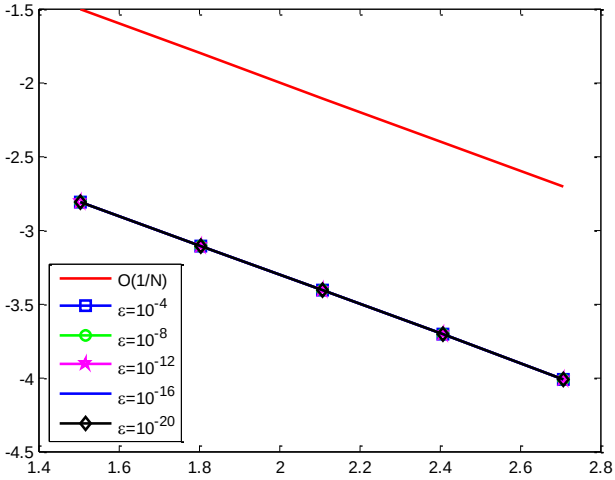

Fig. 6. ε-uniform convergence with NSFDM in Log-Log scale for example 2

7. Discussion and Conclusion

This study introduces fitted operator finite difference numerical method (NSFDM) for solving singularly perturbed delay differential equations with integral boundary condition. The behavior of the continuous solution of the problem is studied and shown that it satisfies the continuous stability estimate and the derivatives of the solution are also bounded. The numerical scheme is developed on uniform mesh using exponential fitted operator in the given differential equation. The integral boundary condition is treated using Simpson's rule. The stability of the developed numerical method is established and its uniform convergence is proved. To validate the applicability of the method, two model problems are considered for numerical experimentation for different values of the perturbation parameter and mesh points. The numerical results are tabulated in terms of maximum absolute errors, numerical rate of convergence and uniform errors (see Tables 1-4). Further, behavior of the numerical solution (Figure 1 and 4), point-wise absolute errors (Figure 2 and 5) and the ε -uniform convergence of the method is shown by the log-log plot (Figure 3 and 6). The method is shown to be ε-uniformly convergent with order of convergence $O(h)$. The performance of the proposed scheme is investigated by comparing with prior study (see Table 2 and 4). The proposed method gives more accurate, stable and ε-uniform numerical result.

Reference

[1] Derstine M. W., Gibbs F.A.H.H.M. and Kaplan D. L., Bifurcation gap in a hybrid optical system, Phys. Rev. A, 26, 3720-3722, 1982.

[2] Longtin A. and J. Milton J., Complex oscillations in the human pupil light reflex with mixed and delayed feedback, Math. Biosci, 90, 183-199, 1988.

[3] Mackey M.C. and Glass L., Oscillation and chaos in physiological control systems, Science. 197, 287-289, 1977.

[4] Mallet-Paret J. and Nussbaum R. D., A differential-delay equations arising in optics and physiology, SIAMJ. Math. Anal. 20, 249-292, 1989.

[5] Lange C.G. and Miura R.M., Singular perturbation analysis of boundary value problems for differential difference equations, SIAM J. Appl. Math. Vol. 42(3), 502-531, 1982.

[6] Kadalbajoo M.K and Sharma K.K., An exponentially fitted finite difference scheme for solving boundary value problems for singularly-perturbed differential-difference equations: small shifts of mixed type with layer behaviour, J. Comput. Anal. Appl. Vol. 8(2), 151-171, 2006.

[7] Patidar K. C. and Sharma K.K., ε-uniformly convergent non-standard finite difference methods for singularly perturbed differential difference equations with small delay, Appl. Math. Comput. Vol. 175(1), 864-890, 2006.

[8] Kadalbajoo M.K. and Sharma K.K., An ε-uniform convergent method for a general boundary-value problem for singularly perturbed differential-difference equations: Small shifts of mixed type with layer behaviour, J. Comput. Methods Sci. Eng, 6, 39-55, 2006.

[9] Kadalbajoo M.K. and Sharma K.K., Numerical treatment of boundary value problems for second order singularly perturbed delay differential equations, Comput. Appl. Math, vol. 24(2), 151-172, 2005.

[10] Kadalbajoo M.K. and Sharma K.K., Numerical treatment for singularly perturbed nonlinear differential difference equations with negative shift, Nonlinear Anal. Theory Methods Appl, vol. 63(5), e1909-e1909, 2005.

[11] Kadalbajoo M.K. and Sharma K.K., Numerical analysis of singularly perturbed delay differential equations with layer behaviour, Appl. Math. Comput, vol. 157(1), 11-28, 2004.

[12] Kadalbajoo M.K. and Sharma K.K., Numerical analysis of boundary-value problems for singularly perturbed differential-difference equations with small shifts of mixed type, J. Optim. Theory Appl, vol.115(1), 145-163, 2002.

[13] Hongijiong T., Numerical methods for singularly perturbed delay differential equations, In proceeding of the International conference on Boundary and Interior Layers, Computational and Asymptotic Methods-BAIL 2004, ONERA, Toulouse.

[14] Amiraliyev G. M and Cimen E., Numerical method for a singularly perturbed convection-diffusion problem with delay, Appl. Math. Comput. 216, 2351-2359, 2010.

[15] Subburayan V. and Ramanujam N., An initial value technique for singularly perturbed convection-diffusion problems with a negative shift, J. Optim Theory Appl. 158, 234-250, 1992.

[16] Sakar E. and Tamilselvan A., Singularly perturbed delay differential equations of convection–diffusion type with integral boundary condition, J. Appl. Math. Comput, 2018, https://doi.org/10.1007/s12190-018-1198-4.

[17] Clavero C., Gracia J.L. and Jorge J.C., High-order numerical methods for one dimensional parabolic singularly perturbed problems with regular layers, Numer. Methods Partial differential equations, vol. 21(1), 149-169, 2005.

[18] OMalley R.E., Singular Perturbation Methods for Ordinary Differential Equations. Springer-Verlag,New York, (1991).

[19] Woldaregay M.M. and Duressa G.F., parameter uniform numerical method for singularly perturbed differential difference equations, J. Nigerian Math. Soc. Vol.38(2), 223-245, 2009.

International Journal of Engineering & Applied Sciences (IJEAS)
Vol.11, Issue 4 (2019) 494-506
http://dx.doi.org/10.24107/ijeas.649330
Int J Eng Appl Sci 11(4) (2019) 494-506

The Kinematics of the East Anatolian Fault Zone, Eastern Turkey and Seismotectonic Implications

Aylin Tan [a*], *Haluk Eyidoğan* [b]

[a] *Institute of Natural Sciences, Main Science Branch of Geophysical Engineering, Sakarya University, 54187, Sakarya, Turkey*

[b] *Altıntepe, Sırmakeş Sokak, No:18, D.5, Maltepe, 34840, İstanbul, Turkey.*

E-mail address: aylin.tan@ogr.sakarya.edu.tr [a*], eyidoganh@gmail.com [b]

ORCID numbers of authors:
0000-0003-0174-5146[a], *0000-0003-4218-5106*[b]

Received date: 20.11.2019
Accepted date: 04.12.2019

Abstract

One of most prominent and active faults in Eastern Turkey is the NE-SW oriented left-lateral strike-slip East Anatolian Fault Zone (EAFZ) with a length of approximately 500 km. In this study, we have examined the recent seismicity of EAFZ that was obtained from the records of 34 three-dimensional broad-band earthquake stations established around the fault zone within TURDEP project since 2006. Further the seismicity and fault mechanism solutions of EAFZ, Eastern Turkey have been examined. The new fault mechanism solutions in addition to previously published 220 earthquakes, with a magnitude of M_L=2.0 or more were determined by a local moment tensor solution and P-wave first motion data. It was suggested that the recent tectonic deformation of EAFZ south of Türkoğlu was taken up by the left-lateral strike-slip active faults in between Amik and Adana Basins were young trans-tensional stress regime was also active.

Keywords: East Anatolian Fault Zone, Earthquake, Fault Mechanism Solution, Stress Tensor Analyses.

1. Introduction

The East Anatolian Fault Zone (EAFZ) is a left-lateral strike-slip fault and 500 km in length. The EAFZ, left lateral active strike-slip fault, extending from Karlıova (Bingöl) at the northeast through İskenderun Gulf at the southwest [1]. The fault starts at the Karlıova triple junction, where it meets the North Anatolian Fault (NAF) to the NE and continues to the Türkoğlu junction (T) (Fig. 1) where it divides into several splays to the SW. It was doubtful whether the continuation of EAFZ towards to southeastern end to the Dead Sea Fault (DSF) or the Cyprus Arc (CA). Various views were proposed: a) the EAFZ continued in southwestern trending from Karlıova to north of Cyprus and was not directly connected to the DSF, b) the Türkoğlu-Amik segment (Karasu Fault Zone) was interpreted as a separate fault, c) the EAFZ continued until Samandağ (Mediterranean Sea) in splay or left-stepping pattern, d) the EAFZ was interpreted as a northward continuation of the DSF [2].

Cilicia region constitutes a wide left lateral shearing zone that indicates a diffuse plate boundary between the African, Arabian and Anatolian plates [3] and [4]. Stress tensor was analyzed and shows that the entire region was under control of the left-lateral strike-slip faulting with minor normal component [5]. The stress tensor for the Osmaniye region showed that the area was affected by E-W oriented extensional stress. Distribution of earthquakes has implied that the splay fault extending from (T) through Andırın to Osmaniye has appeared to be active in this century [5]. The DSF and its junction were with the southern segment of the EAFZ, despite their high tectonic activity was relatively quiescent in the last two centuries [6].

The EAFZ was among the most important active continental transform fault zones in the world as testified by major historical and minor instrumental seismicity [7] outlined the seismological aspects of the region, was outlined that the characteristics of the strong ground motion, the geotechnical characteristics of the region and the structural damages based on site assessments in Elazığ [8]. Some researchers examined that a geochemical investigation has been carried out on the gas phase associated to thermal fluids discharged along three different segments of the EAFZ running from Malatya to the Triple Junction area (Karlıova) where the EAFZ and the NAFZ cross each other [9]. Further a different method, that was Artificial Neural Networks, was studied on EAFZ [10].

In this study, our aim is to examine the seismicity and fault mechanism solutions of EAFZ, eastern Turkey and whether the seismic hazard includes for segments that have been on the EAFZ. The recent seismicity of EAFZ has been monitored using the records of three-dimensional broad-band earthquake stations established around the EAFZ within TURDEP Project since 2006 [11].

2. 3. Method for Stress Tensor Analysis and Fault Mechanism Solutions

The new fault mechanism solutions of 60 earthquakes in addition to previously published 220 earthquake mechanism solutions (total 280) that occurred on and around EAFZ in the time period between 1951 and 2010 were studied to understand the principal stress field and the seismotectonic characteristics along the fault zone that was EAFZ in this study. The magnitude range of the data varied between 2.0 and 7.0. The new fault mechanism solutions in this study were determined by a local moment tensor solution (46) and P-wave first motion data (16) and had the magnitude range of M_L=3.5 or more (Fig. 1). Then we separated the fault zone as 14 parts that were called between D1 and D14, respectively (1 increased-stepped) (Figure 2).

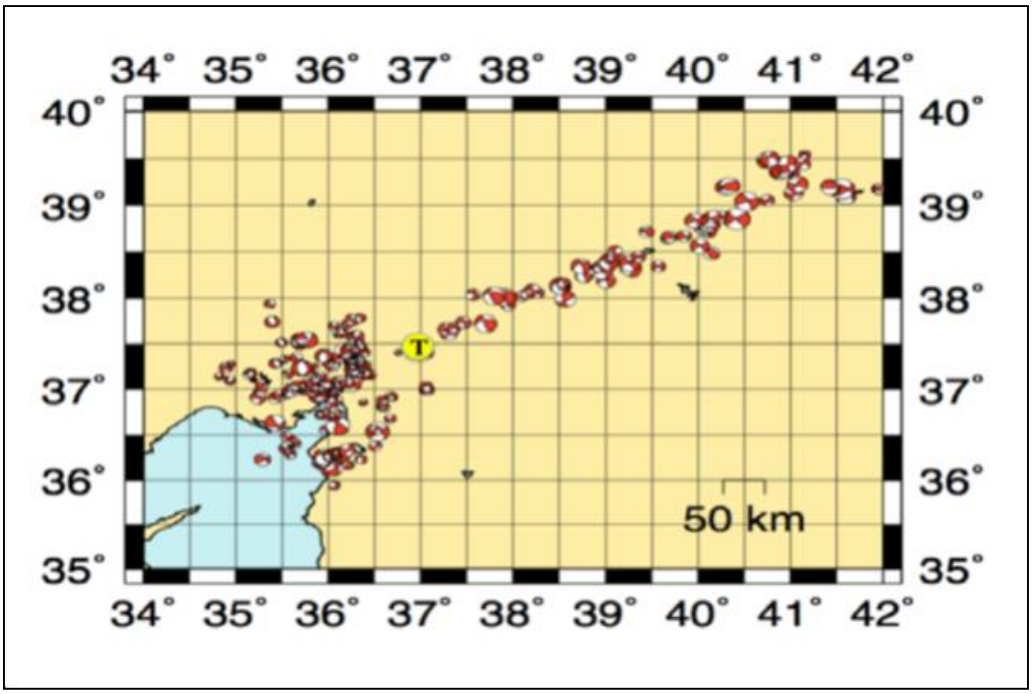

Fig.1. Fault mechanism solutions of 280 events in this study (1951-2010) (The symbol T indicates the location of Türkoğlu junction)

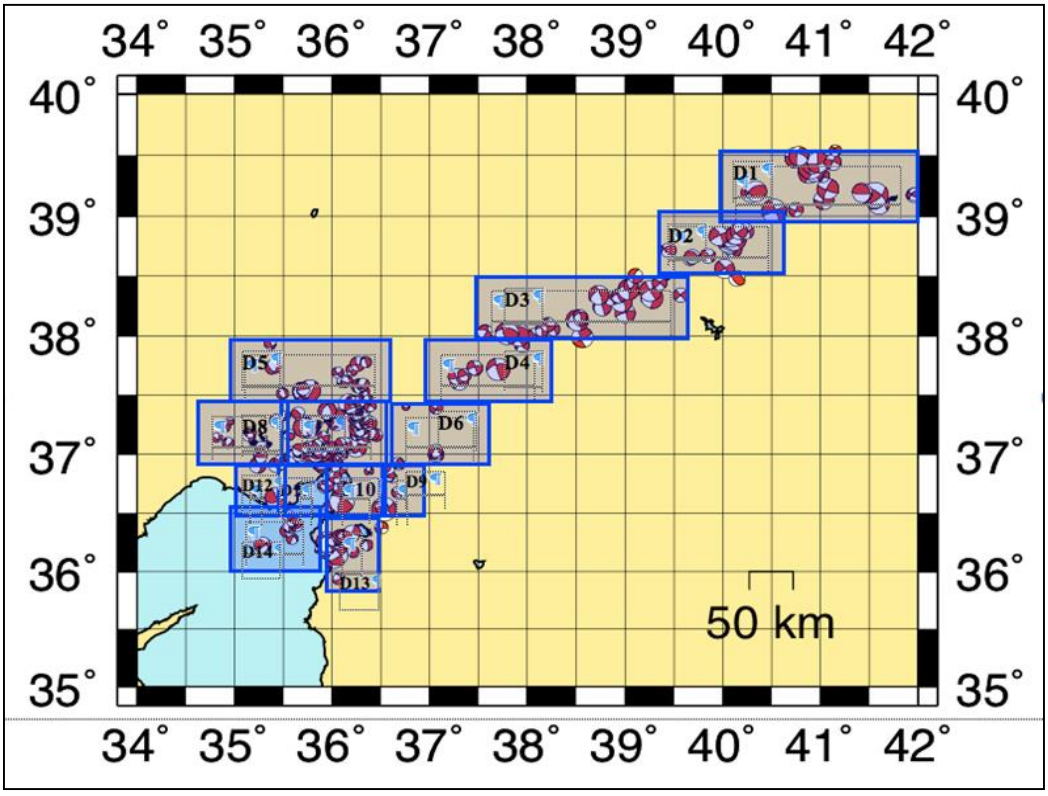

Fig. 2. Segmentation of EAFZ based on the characteristics of 280 earthquake fault mechanism solutions in the years between 1951 and 2010.

The earthquake fault mechanism solutions were divided into sub-regions in order to analyze the tectonic stresses along the EAFZ (Fig. 2). After we separated the segments as 14 parts, we started to apply them the classical Right Dihedron Method. It was improved to estimate the range of tectonic stress regimes using the earthquakes mechanism solutions and geological field data [12]. The Right Dihedron Method was particularly well adapted for the stress inversion of focal mechanisms, as it also used two orthogonal planes to define compressional and extensional quadrants. A stress regime index R' which expressed numerically the stress regime was defined as followed:

R'=R when S1 was vertical (extensional stress regime)

R'=2-R when S2 was vertical (strike-slip stress regime)

R'=2+R when S3 was vertical (compressional stress regime)

where R was the stress ratio and R=(S2-S3)/(S1-S3). Further R' ranged from 0.0 to 3.0 [13] (Fig. 3).

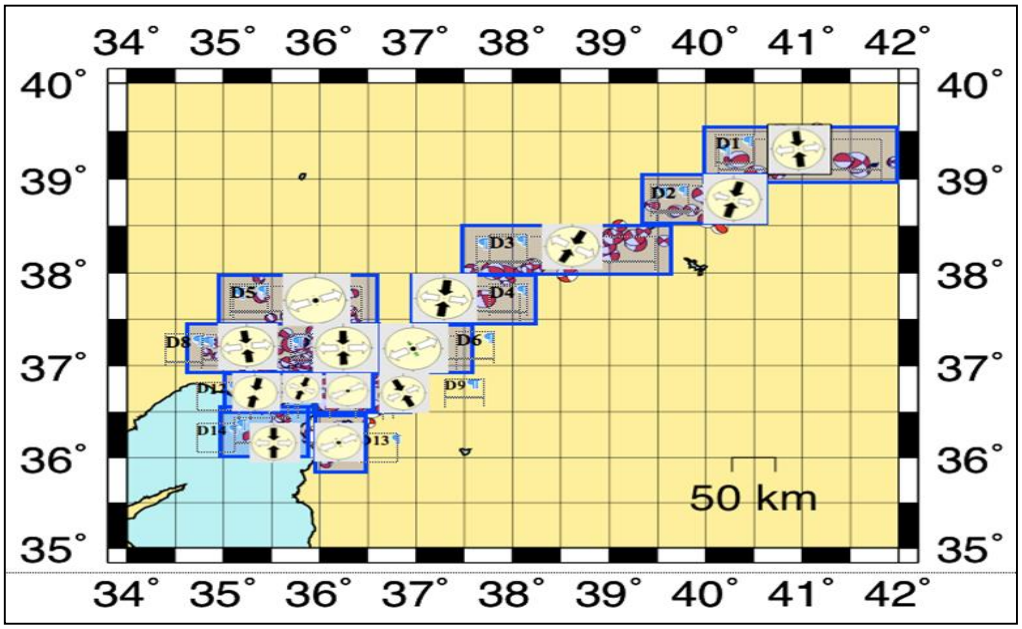

Fig. 3. Analysis using the earthquake mechanism solutions in this study (1951-2010)

The mechanism solutions of 82 earthquakes that were detected by 18 stations between 1993 and 2002 were calculated [3]. They reached the conclusion with the Cilicia region where constituted a wide left lateral shearing zone, indicating a diffuse plate boundary between the African, Arabian and Anatolian Plates (Fig. 4, Fig. 5).

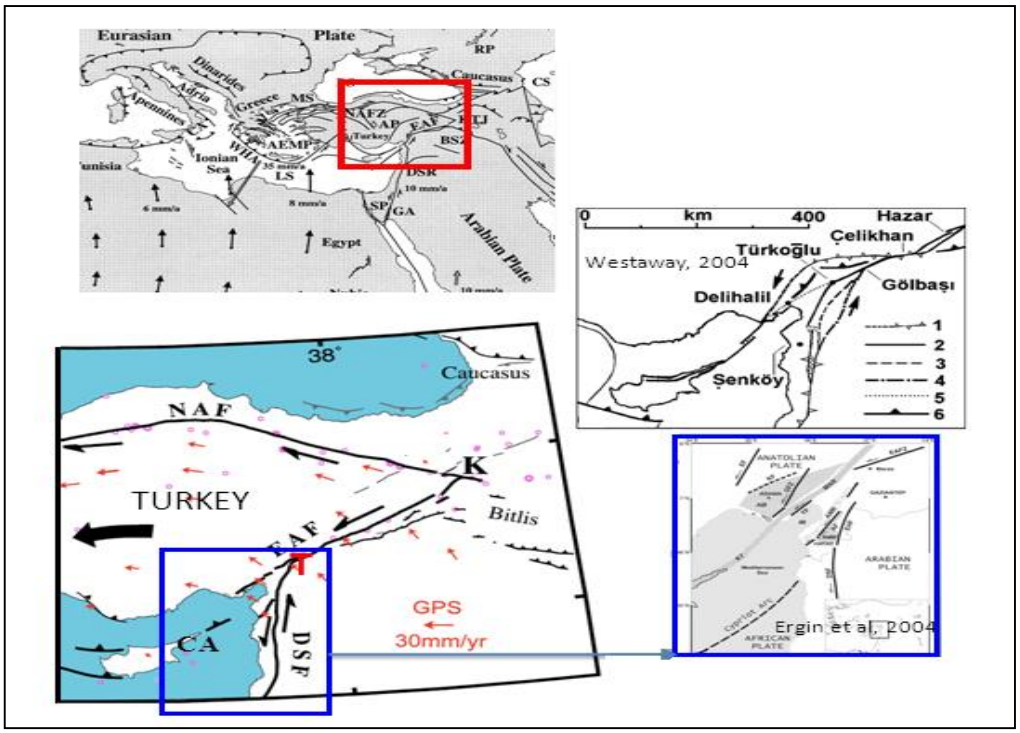

Fig. 4. Study area (Modified from [3] and [4])

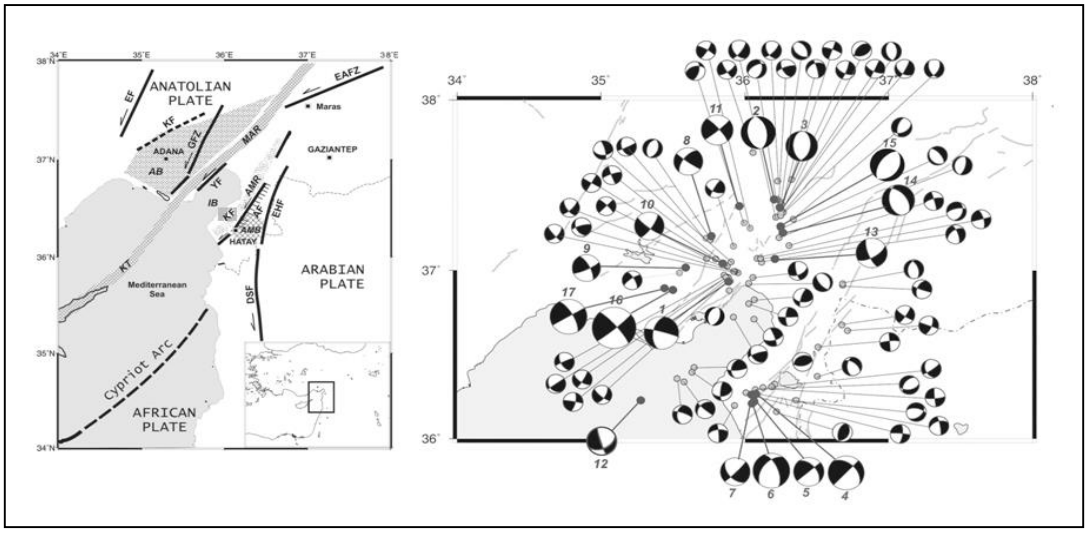

Fig. 5. Focal mechanism solutions that were studied at the study area by [3] (Modified from [3])

Collected earthquake data was analized by TUBITAK-MAM in the Cilician Region between 1999 and the first half of the 2001 (Fig. 6)[5].

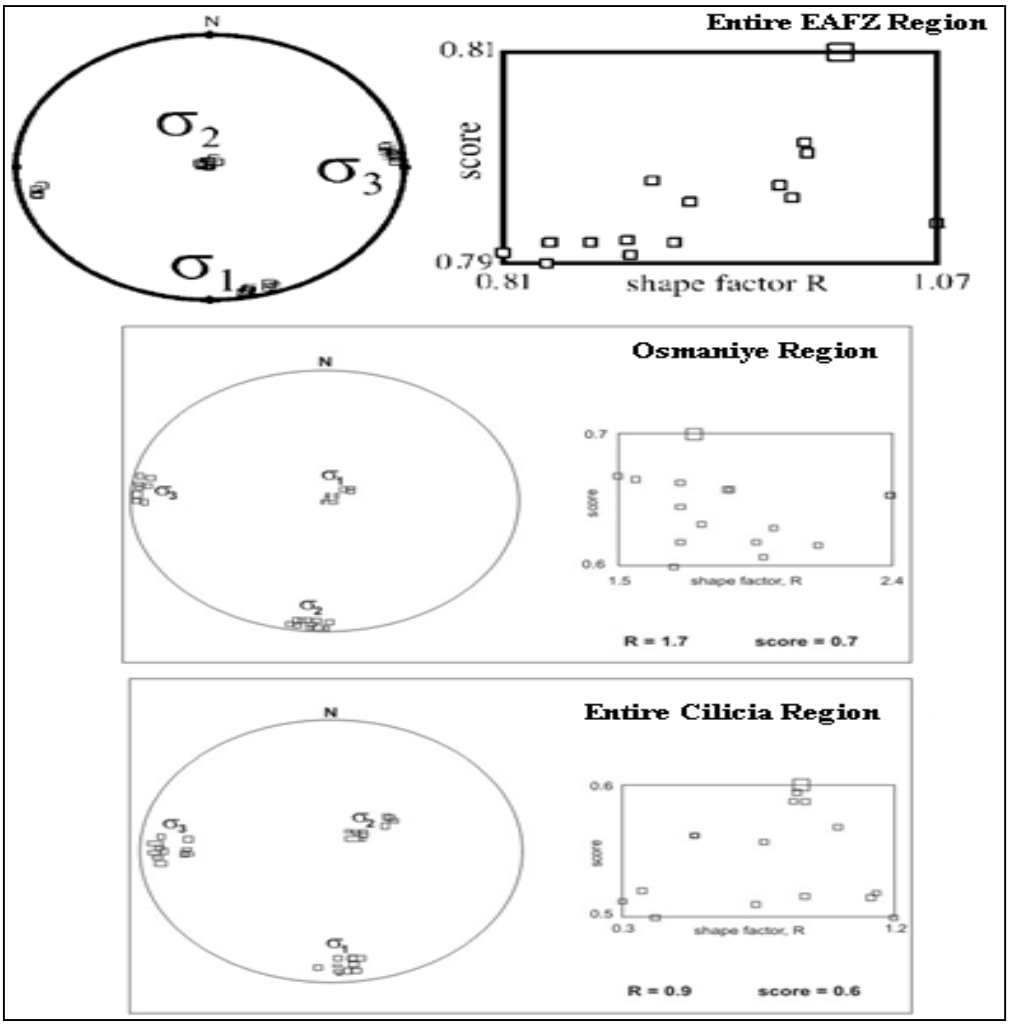

Fig. 6. Analized earthquake data that was collected by TUBITAK-MAM in the Cilician Region between 1999 and the first half of the 2001 by [5]

Stress tensors that were calculated using 59 focal mechanism solutions for the entire Cilicia region. The stress tensors showed that the entire region was under control of the left lateral strike-slip faulting with minor normal component. For the Osmaniye region the stress tensor showed that the area was affected by E-W oriented extensional stress (Fig. 7).

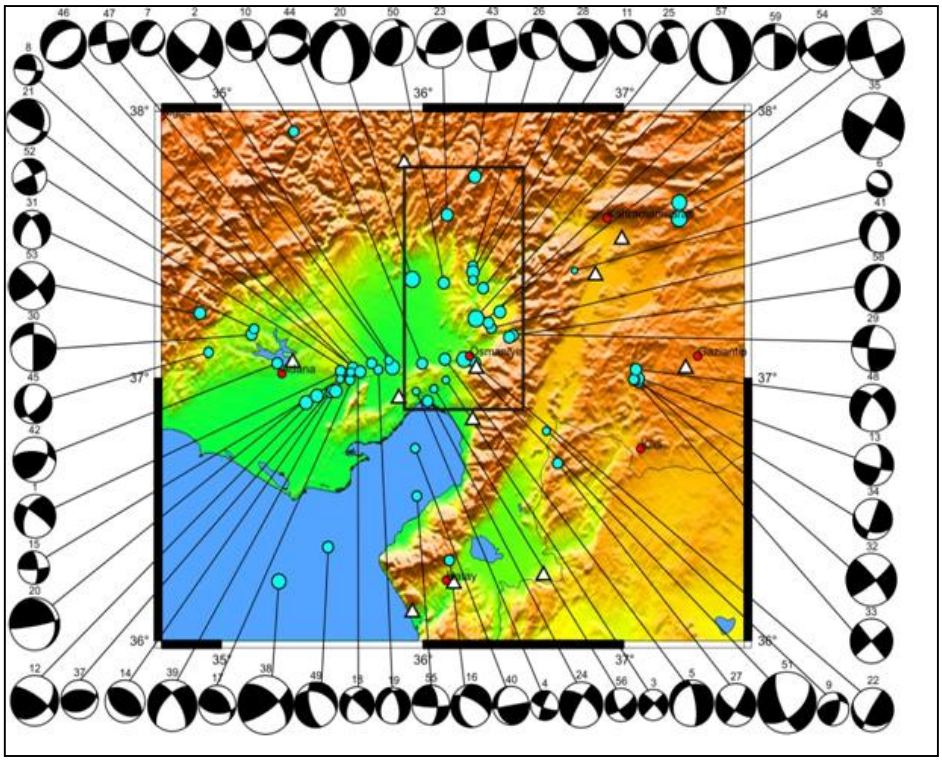

Fig. 7. The stress tensors showed that the Entire EAFZ region, for the Osmaniye region and the Entire Cilicia Region (Modified from [5])

4. Large Earthquakes in the Historical and Instrumental Period at the Study Area

Distribution of earthquakes implied that the splay fault extending from T through Andırın to Osmaniye appeared to be active in this century. Identified areas that had seismicity gaps as Elazığ-Bingöl (EB) Region and Kahramanmaraş-Malatya (KM) Region, respectively according to the Coulomb Stress Change Statement at the study area of the particular seismic risk that was one of them which might be expected to yield a large event [14]. The DSF and its junction with the southern segment of the EAFZ, despite their high tectonic activity was relatively quiescent in the last two centuries [6] (Fig. 8).

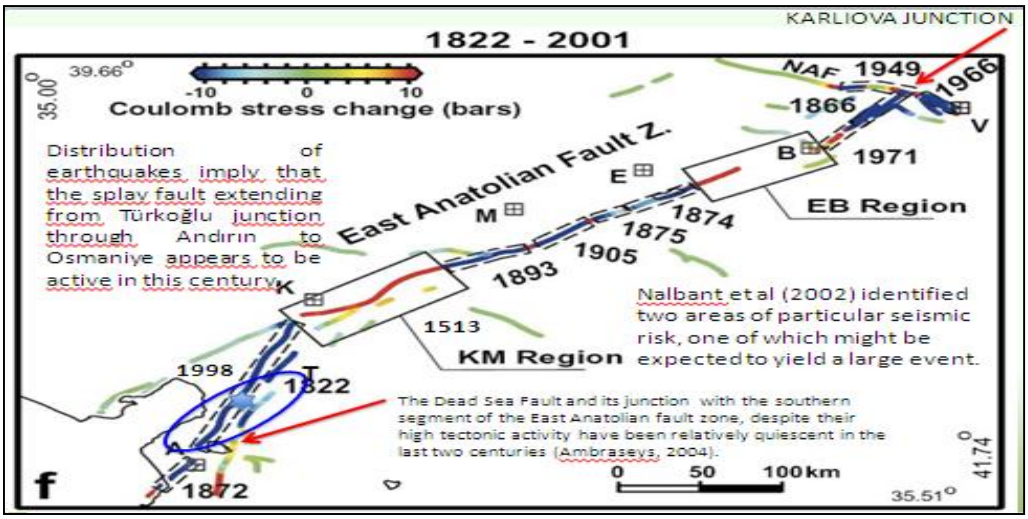

Fig. 8. Coulomb stress change was plotted as a function of distance along EAFZ. Note the spikes along the KM and EB segments at the study area (Modified from [14])

The March 8, 2010 earthquakes that hit Kovancılar and Palu districts of Elazığ province in Turkey. According to United States Geological Survey (USGS), magnitudes of these earthquakes, which caused partial or total collapse in many buildings with life losses, were 6.1 and 5.5, respectively [8]. Further, according to the historical earthquake records, the largest earthquake that affected Palu occurred in 1789 and its intensity is estimated to be 8 and it is stated that 8-10.000 or 51.000 people lost their lives as a result of the earthquake [15]. Some researchers evaluated the failures of masonry and adobe buildings during the June 23, 2011, Maden (Elazığ) earthquake. Maden was a township approximately 80 km away from Elazığ city in Turkey and the magnitude of the earthquake was announced as ML = 5.3 by the Earthquake Division of the Turkish Disaster and Emergency Management Agency (DEMA) [16]. It was an earthquake that might be called as the large earthquake on the EAFZ, too. Another researcher said that recent earthquakes occurred in Bingöl on 22.05.1971, Palu on 25.03.1977, Bingöl on 01.05.2003 and Kovancılar on 08.03.2010 were quite important for Palu and its environs on the EAFZ [17]. On February 21, 2007, a moderate-sized (Mw 5.7) earthquake struck the town of Sivrice (Elazig, Turkey) located within the East Anatolian Fault (EAF) zone that formed the boundary between the Arabian and Anatolian plates [18]. Some reseachers reported that the last recorded large historical earthquake near the study area is the 1513 event, which involved surface faulting between Türkoğlu and Gölbaşı [19].

5. Instrumental Seismicity of EAFZ

There have been three discussion points for determining seismicity gaps: a) the EAFZ continued southwestern trending from Karlıova (K) to Cyprus and has been not directly connected to DSF and c) the EAFZ continued until Samandağ (Mediterranean Sea) in splay or left-stepping pattern. For those reasons we obtained a seismicity map between 1973 and 2009 and determined KM and EB Regions, too (Fig. 9).

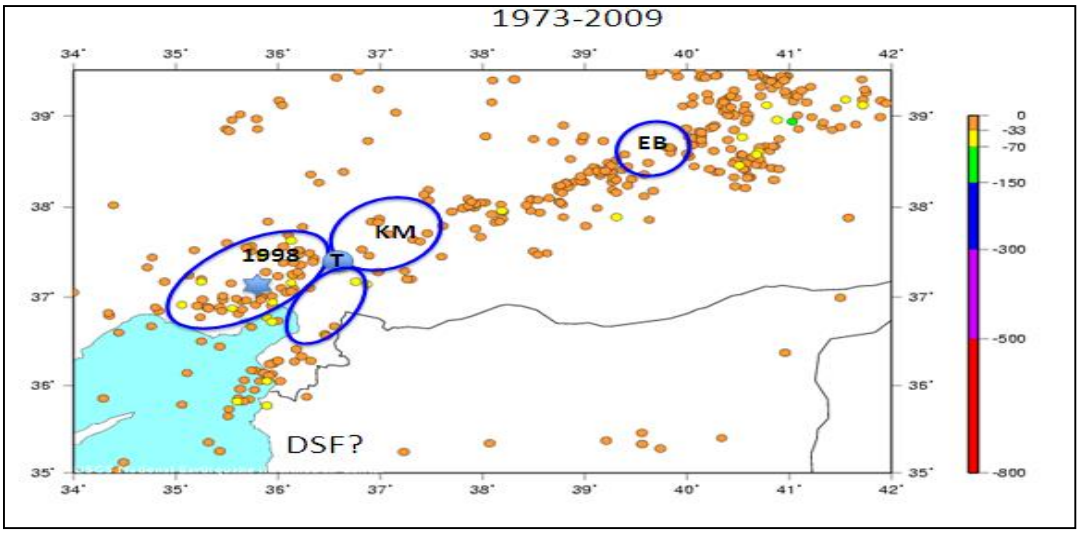

Fig. 9. KM and EB Regions, the Adana Earthquake in 1998 (Mw=6.2) in Adana, Turkey were shown as blue star and seismicity gap between EAFZ and DSF were shown as a blue ecliptic in this study. Earthquake activity was shown in the EAP Region for 50 BC-1994 AD. Circle size correlated with magnitude, color correlated with depth. Largest earthquake with associated magnitude was 7.7. Smallest earthquake with associated magnitude was 4.0. Very small circles had no associated magnitude (Modified [14]).

The recent seismicity of EAFZ had been monitored by using the records of 34 three-dimensional broad-band earthquake stations which were established around the EAFZ within TURDEP Project since 2006 [11]. The coordinates of the error margins of recently relocated epicenters were less than ±2 km. Some epicenter clusters displayed parallel and conjugate fault activity to EAFZ. The EAFZ has had high seismicity for near present time. We can see them on Fig. 10-11-12 and 13, respectively below.

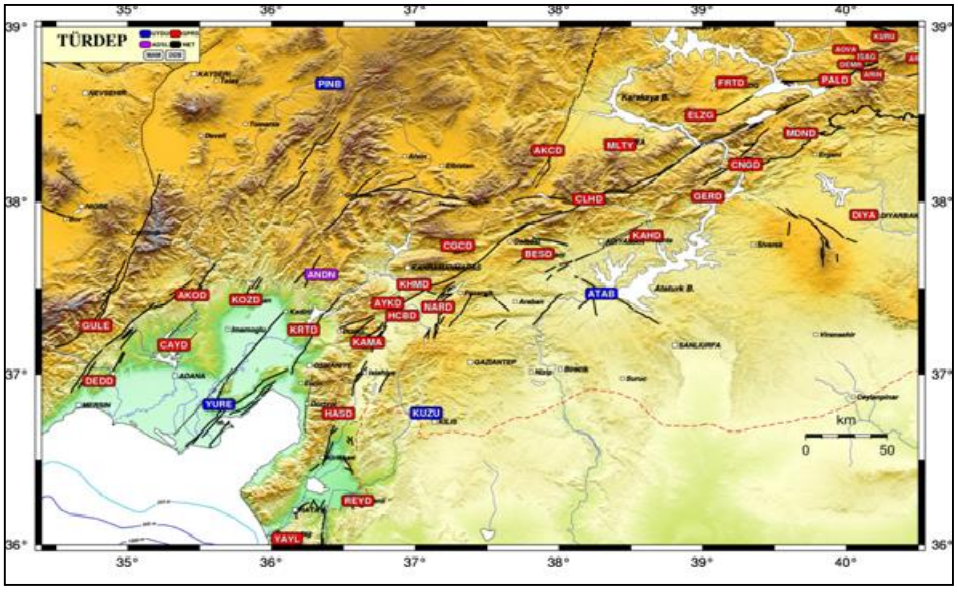

Fig. 10. The earthquake stations at the study area that were located by different institutes [11]

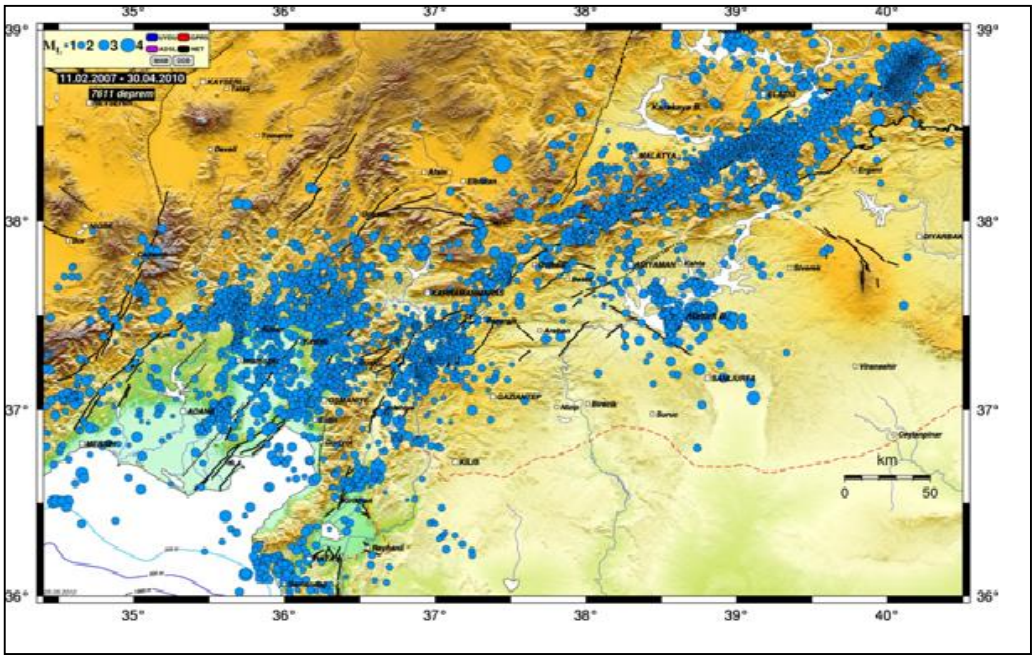

Fig. 11. Earthquakes that were classified according to magnitude scales (ML=1.0, 2.0, 3.0 and 4.0) between 11.02.2007 and 30.04.2010 at TURDEP Project TUBITAK-MAM, Turkey [11]

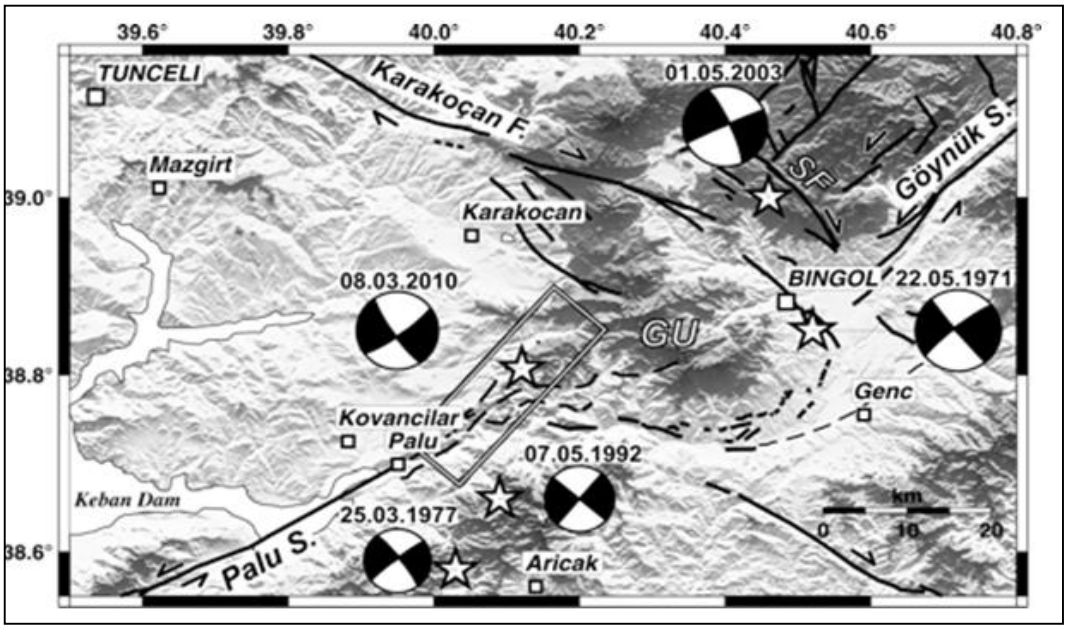

Fig. 12. Focal mechanism solutions of some major and strong earthquakes in vicinity of the study area (Modified from TURDEP Project, TÜBİTAK-MAM [11])

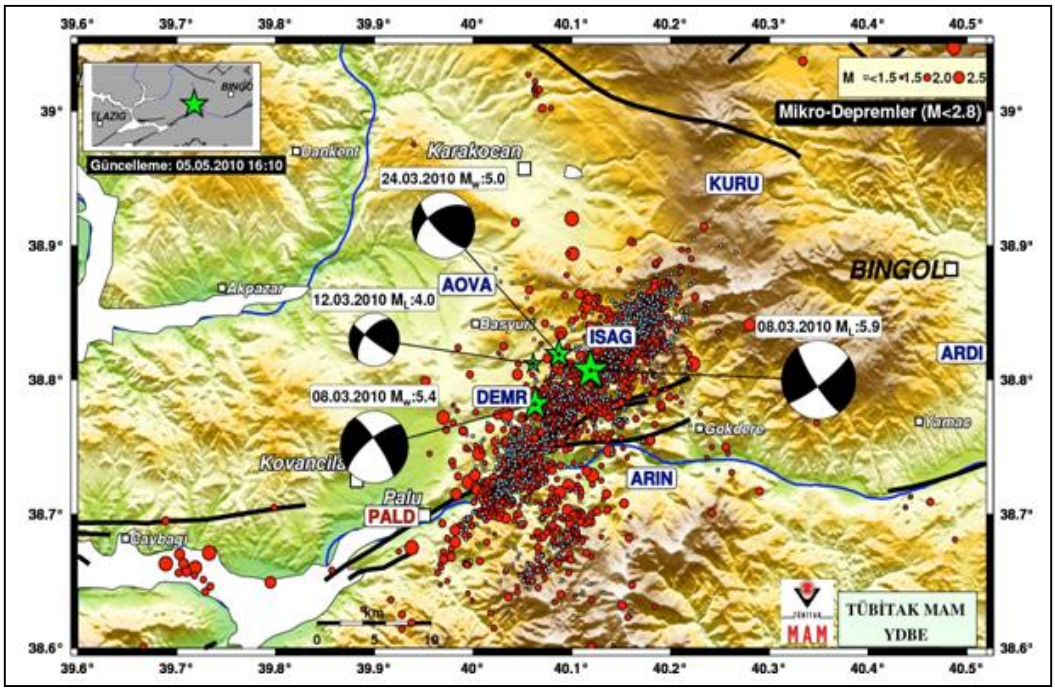

Fig. 13. Southwestern part of region EB has produced an earthquake with M=6.0 on March 8, 2010 (Modified from TURDEP Project, TÜBİTAK-MAM [11])

8. Results and Discussion

1. A pure strike-slip stress deviator characterized by an approximate N-S trending σ1 and an approximate E-W trending σ3 axis for the area between Karlıova and Türkoğlu along the EAFZ (D1, D2, D3, D4) and R'≈1.48-1.57.

2. A pure extensional and qblique extensive stress deviator characterized by an approximate NE-SW trending σ3 for the area between Türkoğlu and northern tip of DSF along western segment of EAFZ (Maraş and Karasu Basin) (D6, D10, D13) and R'≈0.45-1.73.

3. A pure strike-slip stress deviator characterized by an approximate N-S trending σ1 and an approximate E-W trending σ3 axis for the area west Türkoğlu-Osmaniye zone (D7, D8, D9, D11, D12, D14) and R'≈1.38-1.67.

4. Cilicia region constituted a wide left-lateral shearing zone that indicated a diffuse plate boundary between the African, Arabian and Anatolian Plates.

5. The present day stress regime has been extensional and/or trans-tensional in the southern region of the EAFZ between Türkoğlu and Antakya.

6. The strand of the Karasu fault zone in this region has formed a linkage between DSF and EAFZ.

7. The recent tectonic deformation of EAFZ south of Türkoğlu were taken up dominantly by the left- lateral strike-slip active faults in between Amik and Adana Basins that were young

trans-tensional stress regime has been also active. Further the present seismic quiescence was compared with the past activity (paleoseismic and historic) and it indicated that the EAFZ might be ‘‘locked’’ and accumulating elastic strain energy but could move in the near future [7]. There are the seismic gaps on the EAFZ as we explained in this study, too.

8. Left lateral strike-slip character of EAFZ was more dominant at west of Maraş-Antakya, South of T implying that the continuation of EAFZ towards DSF further Türkoğlu has been debatable based on the recent fault mechanism solutions.

Acknowledgments

We thank to TÜBİTAK-MAM because of their supports of knowledge TURDEP Project TÜBİTAK-MAM, Turkey during this study.

References

[1] Köküm, M. and Özçelik, F. 1789 Palu Depremi, Fırat University *Harput Applied and Research Center, International Palu Symposium Proceedings, 11-13 October, 329-337, 2018.*

[2] Rojaya, B., Heimannb, A. and Toprak, V. Neotectonic and volcanic characteristics of the Karasu Fault Zone (Anatolia, Turkey): The transition zone between Dead Sea transform and the East Anatolian fault zone, *Geodinamica Acta*, 14, 1-17, 2001.

[3] Ergin, M., Aktar, M. and Eyidoğan, H. Present-Day seismicity and seismotectonics of the Cilician Basin: Eastern Mediterranean Region of Turkey, *Bulletin of Seismological Society of America*, 94, 3, 930-939, 2004.

[4] Westaway, R. Kinematic consistency between the Dead Sea Fault Zone and the Neogene and Quaternary left-lateral faulting in SE Turkey, *Tectonophysics*, 391, 1-4, 203-237, 2004.

[5] Tan, A., Eyidoğan, H., Tan, O., Pabuccu, Z., Yörük, A. and Geçgel, V. The new fault mechanism solutions of East Anatolian Fault Zone, Eastern Turkey and Seismo-Tectonic Implications, In Proceedings ESC 2010, 6-10 September 2010, Montpellier, France, p. 7, 2010.

[6] Ambraseys, N. N. The 12th century seismic paroxysm in the Middle East: A historical perspective, Annuals of Geophysics, 47, 733-758, 2004.

[7] Çetin, H., Güneyli, H. and Mayer, L. Paleoseismology of the Palu–Lake Hazar segment of the East Anatolian Fault Zone, Turkey, *Tectonophysics*, 374, 163– 197, 2003.

[8] Celep, Z., Erken, A., Taşkın, B., and İlki, A. Failures of masonry and concrete buildings during the March 8, 2010 Kovancılar and Palu (ElazıĞ) Earthquakes in Turkey, *Engineering Failure Analysis*, 18, 868–889, 2011.

[9] Italiano, F., Şaşmaz, A., Yüce, G. and Okan, O. O. Thermal fluids along the East Anatolian Fault Zone (EAFZ): Geochemical features and relationships with the tectonic setting, *Chemical Geology*, 339, 103–114, 2013.

[10] Külahçı, F., İnceöz, M., Doğru, M., Aksoy, E. and Baykara, O., Artificial neural network model for earthquake prediction with radon monitoring, *Applied Radiation and Isotopes*, 67, 212–219, 2009.

[11] http://www.mam.gov.tr/english/YDBE/projeler/Makes-Major.html

[12] Delvaux, D. and Sperner, B. New aspects of tectonic stress inversion with reference to the TENSOR program, NIEUWLAND, D. A. (Ed.) New insights into structural interpretation and modelling, Geological Society, London, *Special Publications* 212,75-100, 2003.

[13] Delvaux, D., Moeys, R., Stapel, G., Petit, C., Levi, K., Miroshnichenko, A., Ruzhich, V. and Sankov, V. Paleostress reconstructions and geodynamics of the Baikal region, Central Asia. Part II: Cenozoic rifting. In: Cloetingh, S., Fernandez, M., Munoz, J.A., Sassi, W. and Horvath, F. (Editors), Structural controls on sedimentary basin formation, *Tectonophysics*, 282, 1-38, 1997.

[14] Nalbant, S. S., McCloskey, J., Steacy, S. and Barka, A.A. Stress accumulation and increased seismic risk in Eastern Turkey, *Sci. Lett*., 195, 291-298, 2002.

[15] Köküm, M. and Özçelik, F. A case study on reassessment of historical earthquakes: 1789 Palu (Elazığ) Earthquake, Eastern Anatolia, Turkey, *Bulletin of the Mineral Research and Exploration*, 161-?, 2020 (Uncorrected Proof).

[16] Sayın, E., Yön, B., Calayır, Y. and Karaton, M., Failures of masonry and adobe buildings during the June 23, 2011 Maden-(Elazığ) earthquake in Turkey, *Engineering Failure Analysis*, 34, 779–791, 2013.

[17] Sunkar, M., Major Earthquakes in The Historical and Instrumental Periods on Palu (Elazığ) and Effects on Settlements, Fırat University Harput Applied and Research Center, *International Palu Symposium Proceedings*, 11-13 October, 297-309, 2018.

[18] Şentürk, S, Çakır, Z., Ergintav, S. and Karabulut, H., Reactivation of the Adıyaman Fault (Turkey) through the Mw 5.7 2007 Sivrice earthquake: An oblique listric normal faulting within the Arabian- Anatolian plate boundary observed by InSAR, *Journal of Geodynamics*, 131, 101654, 2019.

[19] Yönlü, Ö., Altunel, E., Karabacak, V. and Akyüz, H., Evolution of the Gölbaşı basin and its implications for the long-term offset on the East Anatolian Fault Zone, Turkey, *Journal of Geodynamics*, 65, 272– 281, 2013.

International Journal of Engineering & Applied Sciences (IJEAS)
Vol.11, Issue 4 (2019) 507-511
http://dx.doi.org/10.24107/ijeas.655851
Int J Eng Appl Sci 11(4) (2019) 507-511

Comparative Stability Analysis of Silicone Carbide Nanotube using MD Simulation and FEM Software

Kadir Mercan

Department of Civil Eng., Mehmet Akif Ersoy University, Burdur, Turkey

E-mail address: kmercan@mehmetakif.edu.tr

ORCID numbers of authors:
0000-0003-3657-6274

Received date: 17.11.2019
Accepted date: 05.12.2019

Abstract

In this paper, the stability analysis of silicon carbide nanotube (SiCNT) has been investigated. Nanotubes has many advantages with its very high surface area, exceptional electrical conductivity and resistance to high temperature and external loads. Although nanotubes can be obtained without superfluous effort, it is not facile to achieve experimental analyzes due to demand of laboratory equipment with astronomical cost. To obtain critical buckling loads, both molecular dynamic (MD) method and ANSYS finite element software is used in current paper. LAMMPS (Large-scale Atomic/Molecular Massively Parallel Simulator) is used for calculating critical buckling load. Also, VMD (visual molecular dynamics) is used to visualize atoms in molecular dynamic analysis.

Keywords: SiCNT, stability, molecular dynamics, finite element.

1. Introduction

The popularity of nanotube and nanomaterial research and usage has been dramatically raised with the understanding of its gigantic potential and advantages [1-3]. Nanomaterials such as graphene has attracted worldwide attention due to their superior material properties and almost unlimited usage areas such as aerospace, drug delivery, modern automotive technology, high efficiency computers, textile etc. [4-6]. The superiority of nanomaterials comes from its very high surface area, exceptional electrical conductivity and resistance to high temperature and external loads. Outstanding mechanical stiffness and tensile strength put nanomaterials forward to conventional engineering materials. The discovery of Carbon nanotube (CNT) has been composed as a

revolutionary point for many areas. After CNT, new types of nanotubes with superior properties have been produced and used. Most used nanotubes in engineering is CNT, SiCNT, and boron nitride nanotube (BNNT).

Improvement in material and usage of nano-sized materials such as graphene, silicone, CNT, SiCNT (silicon carbide nanotube), etc. resulted in smaller and more effective end products. Comparing nanotubes SiCNT is the one with the highest resistance to heat (1000 ^{o}C in air) and BNNT is the one with highest stiffness with Young modulus 1.8 TPa while CNT can resist temperature up to 600 ^{o}C in air and 1.0 TPa Young modulus. These limits guide researchers and engineers to specify which nanotube to use in different usage areas with different requirements. Because of astronomical cost in building a laboratory with sufficient equipment to perform stability analyzes in nano-size, many computational mechanic methods have been used to make analyzes possible with much lower cost [7].

2. FEM Analysis using ANSYS

The history of finite element method dates back to 1942. Any material in nature eventuate from multiple atoms coming together in a certain order. For SiCNT, these atoms are silicon and carbon atoms bonding in hexagonal shape with 2.29 Å bond length. Finite element method based on modeling the structure by meshing in smaller parts. Results are more satisfactory with finer meshing. In figure 1 the real structure of SiCNT is demonstrated at left side of figure with the finite element (meshed) model at the right side. Meshing is one of the major problem to obtain accurate results. Inaccurate meshing leads inaccurate results in software. As coarse meshing is an issue in meshing, very fine meshing can also end up with very long calculating and simulating period in software.

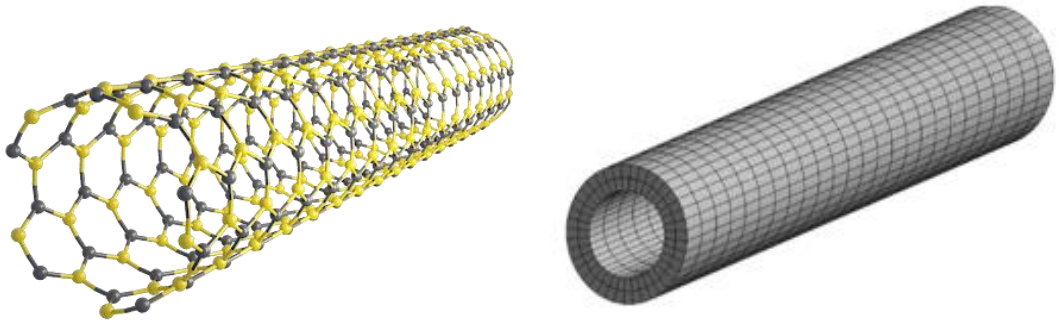

Fig. 1. Real and finite element model of SiCNT

As it can be seen from figure 1, the finite element model used in ANSYS multiphysics consist of a simple tubular structure. SiCNT material properties was applied to the model to obtain critical buckling load.

3. MD Simulation using LAMMPS

Molecular dynamic is an effective and accurate tool to calculate the critical buckling load of nanotubes. LAMMPS open source software is used to perform molecular dynamic simulation. To model interatomic potential function many model has been used such as Tersoff, Tersoff-Brenner, AIREBO (Adaptive Intermolecular Reactive Empirical Bond Order). Models differs from each other in many ways. To illustrate, AIREBO potential is a multi-body force field which is developed for hydrocarbons and includes REBO, Lennard-Jones, torsional potentials as sub-components. Xu *et al.* [8] have demonstrated that AIREBO is able to predict wrinkling patterns in graphene sheets which can be observed in experimental analyzes [9]. Furthermore, Zheng et al. have demonstrated that AIREBO can also capture the hybridization state caused by the deformation-induced curvature [10].

AIREBO potential can be expressed as follows [11]

$$E = \frac{1}{2}\sum_i \sum_{j\neq i}\left(E_{ij}^{REBO} + E_{ij}^{LJ} + \sum_{k\neq i,j}\sum_{l\neq i,j,k} E_{kijl}^{TORS}\right) \tag{1}$$

where

$$E_{ij}^{REBO} = V_{ij}^{R}(r_{i,j}) + b_{i,j}V_{ij}^{A}(r_{i,j}) \tag{2}$$

$$E_{ij}^{LJ} = S\left(t_r(r_{i,j})\right)S\left(t_b(b_{i,j}^{*})\right)C_{i,j}V_{ij}^{LJ}(r_{i,j}) + (1 - S\left(t_r(r_{i,j})\right))C_{i,j}V_{ij}^{LJ}(r_{i,j}) \tag{3}$$

$$E^{TORS} = \frac{1}{2}\sum_i \sum_{j\neq i}\sum_{k\neq i,j}\sum_{l\neq i,j,k} w_{i,j}(r_{i,j})w_{j,k}(r_{j,k})w_{k,l}(r_{k,l})\, V^{TORS}(\omega_{i,j,k,l}) \tag{4}$$

$$V^{TORS}(\omega\ \ ) = \epsilon\left(\frac{256}{405}cos^{10}\left(\frac{\omega}{2}\right) - \frac{1}{10}\right) \tag{5}$$

here V_{ij}^{R} and V_{ij}^{A} are repulsive and attractive pairwise popentials. These potentials can be obtained by atom types and depends on the atomic distance. $S(t)$ is universal switching function.

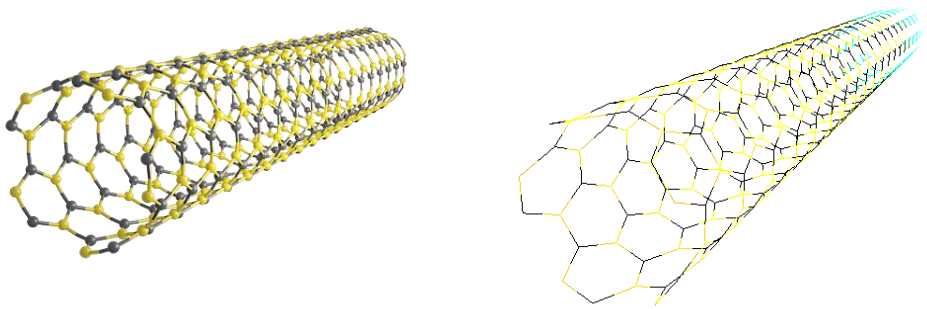

Fig. 1. Real and atomic model of SiCNT

To compare, continuum mechanical models of nanotubes can give accurate results by using size effective theories which take the size effect of nanotubes to improve results by differing the operating equations from classical models and theories [12, 13].

Conclusion

Molecular dynamics simulation method has the advantage of defining every atom of nanotubes and interactions between these atoms. On the other hand, finite element software's are able to model solid or fluid and simulate many scenario leading to perform various analyzes in very short time. Although the speed and ease of finite element software's is attractive, software become insufficient when it comes to model the interaction between atoms. These issue lead to perform analyzes only on perfect (undamaged atoms and interactions) models while the freedom in molecular dynamic is infinite. In experiments which nanotubes are used, it is seen that nanotubes with atomic defects are existing in most experiments caused by limited fabrication technics which means that perfect nanotubes with perfect sequence and bonds is rare in practice. Consequently, although MD simulation has more complications in modeling and performing analyzes compared with finite element softwares, the method has the great advantage of modeling each atoms and bonds separately. This advantage leads to more accurate results.

Reference

[1] Mercan, K., Civalek, O., Buckling analysis of Silicon carbide nanotubes (SiCNTs) with surface effect and nonlocal elasticity using the method of HDQ. *Composites Part B-Engineering*, 114, 35-45, 2017.

[2] Akgoz, B., Civalek, O., Effects of thermal and shear deformation on vibration response of functionally graded thick composite microbeams. *Composites Part B-Engineering*, 129, 77-87, 2017.

[3] Civalek, O., Kiracioglu, O., Free vibration analysis of Timoshenko beams by DSC method. *International Journal for Numerical Methods in Biomedical Engineering*, 26(12), 1890-1898, 2010.

[4] Demir, C., Civalek, O., A new nonlocal FEM via Hermitian cubic shape functions for thermal vibration of nano beams surrounded by an elastic matrix. *Composite Structures*, 168, 872-884, 2017.

[5] Numanoglu, H.M., Akgoz, B., Civalek, O., On dynamic analysis of nanorods. *International Journal of Engineering Science*, 130, 33-50, 2018.

[6] Demir, C., Civalek, O., On the analysis of microbeams. *International Journal of Engineering Science*, 121, 14-33, 2017.

[7] Demir, C., Mercan, K., Numanoglu, H.M., Civalek, O., Bending Response of Nanobeams Resting on Elastic Foundation. *Journal of Applied and Computational Mechanics*, 4(2), 105-114, 2018.

[8] Xu, Z.P., Buehler, M.J., Geometry Controls Conformation of Graphene Sheets: Membranes, Ribbons, and Scrolls. *Acs Nano*, 4(7), 3869-3876, 2010.

[9] Mehralian, F., Beni, Y.T., Molecular dynamics analysis on axial buckling of functionalized carbon nanotubes in thermal environment. *Journal of Molecular Modeling*, 23(12), 2017.

[10] Zheng, Y.P., Xu, L.Q., Fan, Z.Y., Wei, N., Lu, Y., Huang, Z.G., Mechanical Properties of Graphene Nanobuds: A Molecular Dynamics Study. *Current Nanoscience*, 8(1), 89-96, 2012.

[11] Stuart, S.J., Tutein, A.B., Harrison, J.A., A reactive potential for hydrocarbons with intermolecular interactions. *Journal of Chemical Physics*, 112(14), 6472-6486, 2000.

[12] Demir, Ç., Akgöz, B., Erdinç, M.C., Mercan, K., Civalek, Ö., Elastik bir ortamdaki grafen tabakanın titreşim hesabı. *Gazi Üniversitesi Mühendislik-Mimarlık Fakültesi Dergisi*, 32(2), 2017.

[13] Emsen, E., Mercan, K., Akgöz, B., Civalek, Ö., Modal analysis of tapered beam-column embedded in Winkler elastic foundation. *International Journal of Engineering & Applied Sciences*, 7(1), 1-11, 2015.